Development and Validation of a Flight-Identified Full-Envelope Business Jet Simulation Model Using a Stitching Architecture

Tom Berger* and Mark B. Tischler†
U.S. Army Aviation Development Directorate, Moffett Field, CA

Steven G. Hagerott‡
Textron Aviation, Wichita, KS

M. Christopher Cotting§, William R. Gray¶, Capt James L. Gresham‖, Capt Justin E. George**, Capt Kyle J. Krogh**, 1st Lt Alessandro D'Argenio‖, and Capt Justin D. Howland‖
USAF Test Pilot School, Edwards AFB, CA

A full flight-envelope simulation model of the Calspan Variable Stability Learjet-25 was developed from flight data. The model is based on a stitched model architecture, which falls into the class of quasi-Linear-Parameter-Varying models, and was developed using a series of discrete linear point models and trim data. Point models were identified from flight data at five different flight and loading conditions. A scaling method was used and validated to convert all identified point models to the same loading configuration. The quasi-linear aerodynamics from the models were then combined with trim data and the full nonlinear equations of motion to develop the stitched model. Through validation with flight data, the model was shown to accurately represent the aircraft dynamics within the normal flight envelope and be able to estimate the effects of weight and center of gravity variations. The paper provides a brief background of model stitching, lists the steps required to develop a stitched model from flight data, and then demonstrates how the steps are applied to the Learjet.

Nomenclature

0	Subscript denoting trim condition
α	Angle of attack [rad or deg]
β	Angle of sideslip [rad or deg]
Δu	Perturbation controls
Δx	Perturbation states
δ_{a}	Aileron deflection
δ_{e}	Elevator deflection
δ_{f}	Flap deflection
δ_{r}	Rudder deflection
δ_{s}	Stabilator deflection
δ_{T}	Thrust
γ	Flight path angle [rad or deg] or coherence
$\mathcal{M}$	Mass matrix

*Aerospace Engineer, Senior Member AIAA.
†Flight Control Technology Group Leader, Senior Scientist, Associate Fellow AIAA.
‡Senior Engineer Specialist, Senior Member AIAA.
§Master Instructor of Flying Qualities, Associate Fellow AIAA.
¶Chief Test Pilot, Senior Member AIAA.
‖Experimental Flight Test Engineer, Member AIAA.
**Experimental Test Pilot, Member AIAA.

ω Frequency [rad/sec]
ϕ and θ Roll and pitch attitudes [rad or deg]
$\boldsymbol{\rho}$ Vector of scheduling parameters
$\boldsymbol{A}$, $\boldsymbol{B}$, $\boldsymbol{C}$, $\boldsymbol{D}$ State-space matrices
$\boldsymbol{W}$ Vector of states that are not scheduling parameters
$\boldsymbol{X}$, $\boldsymbol{U}$, $\boldsymbol{Y}$ Vectors of states, inputs, and outputs
$\boldsymbol{Z}$ Vector of states that are scheduling parameters
τ Time delay [sec]
a Acceleration [ft/sec^2]
c Mean aerodynamic chord
F Stick force [lbs]
J Frequency response fit cost
J_{RMS} Time domain RMS error cost
L Lift
L, M, N Roll, pitch, and yaw moment derivatives
n Load factor [g]
p, q, r Perturbation roll, pitch, and yaw rates [rad/sec or deg/sec]
t Time [sec]
U, V, W Total x-, y-, and z-body axis velocity [ft/sec]
u, v, w Perturbation x-, y-, and z-body axis velocity [ft/sec]
V_{tot} Total airspeed [ft/sec]
X, Y, Z Longitudinal, lateral, and vertical force derivatives
X_{cg} Longitudinal CG location [ft]
X_{np} Longitudinal neutral point location [ft]
CG Center of Gravity
LSS Longitudinal Speed Stability
MAC Mean Aerodynamic Chord
MTOW Maximum Take-Off Weight
PTI Programmed Test Input
TT Subscript denoting fuel Tip Tank parameter
VSS Variable Stability System

I. Introduction

System identification of the Calspan Variable Stability System (VSS) Learjet LJ-25D was conducted as part of a U.S. Army Aviation Development Directorate (ADD)/Textron Aviation collaborative project with the USAF Test Pilot School (TPS). The project was to develop a full flight-envelope "stitched" simulation model[1,2,3] to accurately represent the LJ-25 flight dynamics and trim characteristics across its flight and loading envelopes. The stitched model refers to a full fight-envelope, real-time simulation model composed of individual linear models and trim data for discrete flight conditions. The model has been used for control law development[4] and has been integrated into the USAF TPS flight simulator laborary.[5]

Zivan and Tischler[1] presented the development of a stitched model from flight data for a Bell 206. In addition, a stitched model of the Cessna CitationJet CJ1 business jet was previously developed from a high-fidelity nonlinear simulation model of the CJ1 (that was not capable of real-time operation) and validated with back-to-back flight and simulator testing.[6] The LJ-25 model presented here was developed and validated from flight data. A significant part of this effort was in developing the necessary methodology for developing a stitched model from flight data.

A flight test campaign was carried out during May 2015 which consisted of four two-hour flights. The data gathered consisted of piloted frequency sweeps, doublets, longitudinal speed stability, steady heading sideslip, and trim data. Data were collected at five flight conditions for model development, and an additional two flight conditions for model validation. As part of a separate flight test conducted in March 2016, additional validation flight data were gathered.

This paper lays out the steps to develop a full flight-envelope stitched model using flight data, and describes how they were applied to the LJ-25. First, individual point models were identified at each flight condition using frequency-domain system identification techniques.[3] Second, the identified models which

were each flown at a unique loading configuration [weight, center of gravity (CG), and inertia] were scaled to a common loading configuration. This was especially important for the Learjet, since the aircraft has large fuel tanks on the tips of its wings which significantly change its roll and yaw moments of inertia, and hence the lateral/directional dynamics. Finally, the models and trim data were "stitched"[2] together into the full flight-envelope model. This stitching technique refers to combining together individual linear models and trim data for discrete flight conditions with the full nonlinear equations of motion to produce a continuous, full fight-envelope simulation model. This type of model is in the class of quasi-linear-parameter-varying (qLPV) models,[7] which is discussed in more detail in Section II.

A brief description of model stitching is presented in Section II. Section III provides a description of the aircraft and flight test. Then, identification results of one individual point model will be presented in Section IV, followed by a method to baseline a point model from one loading configuration to another in Section V. Section VI described a method to repurpose longitudinal speed stability data to trim data for use in the stitched model. Finally, the results of the stitched model will be presented in Section VII, including comparison with validation flight data in Section VIII .

II. Model Stitching Overview

A continuous, full-envelope simulation model of the LJ-25 was developed to represent the aircraft dynamics accurately over its entire flight and loading envelopes. This was accomplished using the model stitching technique,[2,3] which refers to the process of combining a collection of linear state-space models at various fight conditions with trim data into a full-envelope simulation model. At its core, the stitched model is comprised of a quasi-linear-parameter-varying model (qLPV), with distinctive features specific to aircraft and rotorcraft applications. This section will provide some background on qLPV models and detail how the stitched model is an extension of the qLPV framework with aircraft-specific features.

A. Quasi-Linear-Parameter-Varying Model

Linear-parameter-varying (LPV) models or systems are, in general, representations of nonlinear systems:

$$\dot{\boldsymbol{X}}(t) = f\big(\boldsymbol{X}(t),\boldsymbol{U}(t)\big) \tag{1}$$
$$\boldsymbol{Y}(t) = h\big(\boldsymbol{X}(t),\boldsymbol{U}(t)\big) \tag{2}$$

where:

$\boldsymbol{X}$, $\boldsymbol{U}$, and $\boldsymbol{Y}$ are the total states, inputs, and outputs of the system, respectively, and
f and h are nonlinear functions.

A LPV model is a linearized state-space representation of the nonlinear system in Equations 1 and 2, but differs from a typical Linear Time Invariant (LTI) system in that its state-space entries are continuous functions of a time-varying scheduling parameter vector $\boldsymbol{\rho}(t)$:[7]

$$\dot{\boldsymbol{X}}(t) = \boldsymbol{A}\big(\boldsymbol{\rho}(t)\big)\Big(\boldsymbol{X}(t)-\boldsymbol{X}_0\big(\boldsymbol{\rho}(t)\big)\Big)+\boldsymbol{B}\big(\boldsymbol{\rho}(t)\big)\Big(\boldsymbol{U}(t)-\boldsymbol{U}_0\big(\boldsymbol{\rho}(t)\big)\Big) \tag{3}$$
$$\boldsymbol{Y}(t) = \boldsymbol{C}\big(\boldsymbol{\rho}(t)\big)\Big(\boldsymbol{X}(t)-\boldsymbol{X}_0\big(\boldsymbol{\rho}(t)\big)\Big)+\boldsymbol{D}\big(\boldsymbol{\rho}(t)\big)\Big(\boldsymbol{U}(t)-\boldsymbol{U}_0\big(\boldsymbol{\rho}(t)\big)\Big)+\boldsymbol{Y}_0\big(\boldsymbol{\rho}(t)\big) \tag{4}$$

where:

$\boldsymbol{A}$, $\boldsymbol{B}$, $\boldsymbol{C}$, and $\boldsymbol{D}$ are the state-space matrices (linearized representations of f and h in Equations 1 and 2 about a trim condition),
$\boldsymbol{\rho}$ is the vector of scheduling parameters,
$\boldsymbol{X}$, $\boldsymbol{U}$, and $\boldsymbol{Y}$ are the total states, inputs, and outputs of the system, respectively,
$\boldsymbol{X}_0$, $\boldsymbol{U}_0$, and $\boldsymbol{Y}_0$ are the trim states, inputs, and outputs of the system, respectively, and
$\dot{\boldsymbol{X}}_0 = 0$ and hence is eliminated from Equation 3.

Thus, the LPV model is a collection of *point models* and trim data at a series of trim scheduling parameter $\boldsymbol{\rho}_0$ values (i.e., $\boldsymbol{A}|_{\boldsymbol{\rho}_0}$, $\boldsymbol{B}|_{\boldsymbol{\rho}_0}$, $\boldsymbol{C}|_{\boldsymbol{\rho}_0}$, $\boldsymbol{D}|_{\boldsymbol{\rho}_0}$, and $\boldsymbol{X}_0|_{\boldsymbol{\rho}_0}$, $\boldsymbol{U}_0|_{\boldsymbol{\rho}_0}$, $\boldsymbol{Y}_0|_{\boldsymbol{\rho}_0}$, respectively) combined into lookup tables.

Note that the number of point models and trim data points do no have to be equal. In fact, it will be shown that it is desirable to have trim data at a finer grid of scheduling parameters values than point models.

If the scheduling parameter vector $\boldsymbol{\rho}$ contains any states of the system (elements of $\boldsymbol{X}$ in Equation 3), then the system is quasi-LPV (qLPV), and is said to be "stitched"[1] in those states. As such, a qLPV system is *stitched* in elements of $\boldsymbol{\rho}$ that are states of the system and *scheduled* in elements of $\boldsymbol{\rho}$ that are not states of the system.

For a qLPV model then, the state vector $\boldsymbol{X}$ can be separated into states that are stitching parameters ($\boldsymbol{Z} \subset \boldsymbol{\rho}$) and states that are not ($\boldsymbol{W} \not\subset \boldsymbol{\rho}$):

$$\boldsymbol{X} = \begin{bmatrix} \boldsymbol{Z} & \boldsymbol{W} \end{bmatrix}^T \tag{5}$$

Then, Equation 3 can be rewritten as (dropping the notation for the dependence on time for brevity):

$$\begin{bmatrix} \dot{\boldsymbol{Z}} \\ \dot{\boldsymbol{W}} \end{bmatrix} = \begin{bmatrix} \boldsymbol{A}_{11}(\boldsymbol{\rho}) & \boldsymbol{A}_{12}(\boldsymbol{\rho}) \\ \boldsymbol{A}_{21}(\boldsymbol{\rho}) & \boldsymbol{A}_{22}(\boldsymbol{\rho}) \end{bmatrix} \begin{bmatrix} \boldsymbol{Z} - \boldsymbol{Z}_0(\boldsymbol{\rho}) \\ \boldsymbol{W} - \boldsymbol{W}_0(\boldsymbol{\rho}) \end{bmatrix} + \begin{bmatrix} \boldsymbol{B}_1(\boldsymbol{\rho}) \\ \boldsymbol{B}_2(\boldsymbol{\rho}) \end{bmatrix} \begin{bmatrix} \boldsymbol{U} - \boldsymbol{U}_0(\boldsymbol{\rho}) \end{bmatrix} \tag{6}$$

Since $\boldsymbol{Z}$ is a stitching parameter, $\boldsymbol{Z}_0(\boldsymbol{\rho}) = \boldsymbol{Z}$ at all times, and Equation 6 becomes:

$$\begin{bmatrix} \dot{\boldsymbol{Z}} \\ \dot{\boldsymbol{W}} \end{bmatrix} = \begin{bmatrix} \boldsymbol{A}_{11}(\boldsymbol{\rho}) & \boldsymbol{A}_{12}(\boldsymbol{\rho}) \\ \boldsymbol{A}_{21}(\boldsymbol{\rho}) & \boldsymbol{A}_{22}(\boldsymbol{\rho}) \end{bmatrix} \begin{bmatrix} \boldsymbol{0} \\ \boldsymbol{W} - \boldsymbol{W}_0(\boldsymbol{\rho}) \end{bmatrix} + \begin{bmatrix} \boldsymbol{B}_1(\boldsymbol{\rho}) \\ \boldsymbol{B}_2(\boldsymbol{\rho}) \end{bmatrix} \begin{bmatrix} \boldsymbol{U} - \boldsymbol{U}_0(\boldsymbol{\rho}) \end{bmatrix} \tag{7}$$

The contributions of $\boldsymbol{A}_{11}$ and $\boldsymbol{A}_{21}$ to $\dot{\boldsymbol{Z}}$ appear to be eliminated from the qLPV model of Equation 7. However, these contributions can be shown to be preserved implicitly through the trim state and input gradients. Starting with the definition of $\boldsymbol{A}_{11}$ as the gradient of $\dot{\boldsymbol{Z}}$ with respect to $\boldsymbol{Z}$ about some trim point $\boldsymbol{\rho}_0$:

$$\boldsymbol{A}_{11} = \left.\frac{\partial \dot{\boldsymbol{Z}}}{\partial \boldsymbol{Z}}\right|_{\boldsymbol{\rho}_0} \tag{8}$$

Next, taking the partial derivative of $\dot{\boldsymbol{Z}}$ from Equation 7 with respect to $\boldsymbol{Z}$ results in:

$$\begin{aligned} \left.\frac{\partial \dot{\boldsymbol{Z}}}{\partial \boldsymbol{Z}}\right|_{\boldsymbol{\rho}_0} = \; & \left.\frac{\partial \boldsymbol{A}_{12}(\boldsymbol{\rho})}{\partial \boldsymbol{Z}}\right|_{\boldsymbol{\rho}_0} [\boldsymbol{W}|_{\boldsymbol{\rho}_0} - \boldsymbol{W}_0(\boldsymbol{\rho}_0)] + \boldsymbol{A}_{12}(\boldsymbol{\rho}_0) \left[\left.\frac{\partial \boldsymbol{W}}{\partial \boldsymbol{Z}}\right|_{\boldsymbol{\rho}_0} - \left.\frac{\partial \boldsymbol{W}_0(\boldsymbol{\rho})}{\partial \boldsymbol{Z}}\right|_{\boldsymbol{\rho}_0} \right] \\ & + \left.\frac{\partial \boldsymbol{B}_1(\boldsymbol{\rho})}{\partial \boldsymbol{Z}}\right|_{\boldsymbol{\rho}_0} [\boldsymbol{U}|_{\boldsymbol{\rho}_0} - \boldsymbol{U}_0(\boldsymbol{\rho}_0)] + \boldsymbol{B}_1(\boldsymbol{\rho}_0) \left[\left.\frac{\partial \boldsymbol{U}}{\partial \boldsymbol{Z}}\right|_{\boldsymbol{\rho}_0} - \left.\frac{\partial \boldsymbol{U}_0(\boldsymbol{\rho})}{\partial \boldsymbol{Z}}\right|_{\boldsymbol{\rho}_0} \right] \end{aligned} \tag{9}$$

Several terms can be canceled out from Equation 9. First, since $\boldsymbol{\rho}_0$ is a trim condition, $\boldsymbol{W}|_{\boldsymbol{\rho}_0} = \boldsymbol{W}_0(\boldsymbol{\rho}_0)$ and $\boldsymbol{U}|_{\boldsymbol{\rho}_0} = \boldsymbol{U}_0(\boldsymbol{\rho}_0)$. Furthermore, $\boldsymbol{W}$ and $\boldsymbol{U}$ are independent of $\boldsymbol{Z}$, so $\partial \boldsymbol{W}/\partial \boldsymbol{Z} = \partial \boldsymbol{U}/\partial \boldsymbol{Z} = 0$. Combining Equations 8 and 9 allows us to calculate an effective qLPV $\boldsymbol{A}_{11}$:

$$\boldsymbol{A}_{11_{\text{qLPV}}} = -\boldsymbol{A}_{12}(\boldsymbol{\rho}_0) \left[\left.\frac{\partial \boldsymbol{W}_0(\boldsymbol{\rho})}{\partial \boldsymbol{Z}}\right|_{\boldsymbol{\rho}_0} \right] - \boldsymbol{B}_1(\boldsymbol{\rho}_0) \left[\left.\frac{\partial \boldsymbol{U}_0(\boldsymbol{\rho})}{\partial \boldsymbol{Z}}\right|_{\boldsymbol{\rho}_0} \right] \tag{10}$$

This shows that the contribution of $\boldsymbol{A}_{11}$ to $\dot{\boldsymbol{Z}}$ is indeed preserved implicitly through the trim state and trim input gradients:

$$\frac{\partial \boldsymbol{W}_0(\boldsymbol{\rho})}{\partial \boldsymbol{Z}} \text{ and } \frac{\partial \boldsymbol{U}_0(\boldsymbol{\rho})}{\partial \boldsymbol{Z}} \tag{11}$$

A similar analysis can be done to show that the contribution of $\boldsymbol{A}_{21}$ is preserved as well.

This may seem like a subtle nuance of qLPV modeling, but understanding its implications is vital to the development of an accurate stitched model. First, it is important to have a fine grid of trim data about each individual point model that not only captures the absolute trim value at the point model condition, but also accurately represents the trim gradients around the point model condition. Second, there should be an internal consistency between the values of $\boldsymbol{A}_{11}$ and $\boldsymbol{A}_{21}$ at each point model and the trim gradients about each point model, to ensure that $\boldsymbol{A}_{11_{\text{qLPV}}}$ will equal $\boldsymbol{A}_{11}$ and $\boldsymbol{A}_{21_{\text{qLPV}}}$ will equal $\boldsymbol{A}_{21}$.

B. Stitched Model

The stitched model applies qLPV modeling specifically to aircraft and rotorcraft with several main distinctions or features relevant to these applications:

1) The first distinction is that the primary scheduling parameter in the stitched model is the total instantaneous x-body axis velocity state U (note the lack of bold, differentiating U, the x-body axis velocity state from $\boldsymbol{U}$, the vector of inputs). The total instantaneous x-body axis velocity state U can be considered to be the true airspeed for typical angle of attack ranges. The stitched model, therefore, is a qLPV model that is stitched in U. For aircraft applications then, Equation 10 above reduces to:

$$X_{u_{\text{qLPV}}} = -X_w(U_0)\frac{\partial W}{\partial U}\bigg|_{U_0} + g\cos\Theta_0\frac{\partial \Theta}{\partial U}\bigg|_{U_0} - X_{\delta_\text{e}}(U_0)\frac{\partial \delta_\text{e}}{\partial U}\bigg|_{U_0} - X_{\delta_\text{T}}(U_0)\frac{\partial \delta_\text{T}}{\partial U}\bigg|_{U_0} \tag{12}$$

$$Z_{u_{\text{qLPV}}} = -Z_w(U_0)\frac{\partial W}{\partial U}\bigg|_{U_0} + g\sin\Theta_0\frac{\partial \Theta}{\partial U}\bigg|_{U_0} - Z_{\delta_\text{e}}(U_0)\frac{\partial \delta_\text{e}}{\partial U}\bigg|_{U_0} - Z_{\delta_\text{T}}(U_0)\frac{\partial \delta_\text{T}}{\partial U}\bigg|_{U_0} \tag{13}$$

$$M_{u_{\text{qLPV}}} = -M_w(U_0)\frac{\partial W}{\partial U}\bigg|_{U_0} - M_{\delta_\text{e}}(U_0)\frac{\partial \delta_\text{e}}{\partial U}\bigg|_{U_0} - M_{\delta_\text{T}}(U_0)\frac{\partial \delta_\text{T}}{\partial U}\bigg|_{U_0} \tag{14}$$

Again, this shows the importance of having a fine grid of trim data around each point model to accurately

Generally, the stitched model scheduling parameter vector can include additional state-elements (stitching elements, $\subset \boldsymbol{X}$), such as y-body axis velocity V in the case of rotorcraft applications,[2] and exogenous-elements (scheduling parameters, $\not\subset \boldsymbol{X}$), such as flap deflection δ_f in the case of fixed-wing applications or nacelle angle in the case of tilt-rotor applications.[8] When state-space matrices and trim data are available at multiple altitudes, then altitude may be be included as a scheduling parameter.

2) The second distinction of the stitched model is that when state-space matrices and trim data are only available at a single altitude, the stitched model can apply air density ratio scaling. This allows the stitched model to account for variations in trim and dynamics with altitude, without explicitly including altitude in the schedule parameter vector. This was the case for the LJ-25 application presented herein, where the model is stitched with x-body axis velocity state U and scheduled with flap deflection δ_f, only:

$$\boldsymbol{\rho} = \begin{bmatrix} U & \delta_\text{f} \end{bmatrix}^T \tag{15}$$

Therefore, for the LJ-25 application, the state trim values ($\boldsymbol{X}_0$ in Equation 3) and control input trim values ($\boldsymbol{U}_0$ in Equation 3) are implemented as lookup tables with respect to U and δ_f.

Note that a limitation of air density ratio scaling is in preserving Mach effects with altitude, since it does not capture the changing Mach number for a given airspeed with changing altitude. Therefore, when Mach effects are important, it is advisable to include altitude as a scheduling parameter by having point models at multiple altitudes.

3) The third distinction of the stitched model is the recognition that the general state-space form of Equation 3 describes aircraft-specific forces and moments, which can be broken up into their respective aerodynamic, gravity, and Coriolis components:

$$\begin{aligned}\dot{\boldsymbol{X}} = {} & \boldsymbol{A}_{\text{aero}}(\boldsymbol{\rho})\big(\boldsymbol{X} - \boldsymbol{X}_0(\boldsymbol{\rho})\big) + \boldsymbol{A}_{\text{grav}}(\boldsymbol{\rho})\big(\boldsymbol{X} - \boldsymbol{X}_0(\boldsymbol{\rho})\big) \\ & + \boldsymbol{A}_{\text{Cor}}(\boldsymbol{\rho})\big(\boldsymbol{X} - \boldsymbol{X}_0(\boldsymbol{\rho})\big) + \boldsymbol{B}_{\text{aero}}(\boldsymbol{\rho})\big(\boldsymbol{U} - \boldsymbol{U}_0(\boldsymbol{\rho})\big)\end{aligned} \tag{16}$$

In the stitched model, only the aerodynamic components ($\boldsymbol{A}_{\text{aero}}$ and $\boldsymbol{B}_{\text{aero}}$ in Equation 16) are implemented as lookup tables with respect to $\boldsymbol{\rho}$. The gravity component and Coriolis terms ($\boldsymbol{A}_{\text{grav}}$ and $\boldsymbol{A}_{\text{Cor}}$ in Equation 16) are removed from the linear point models and included instead in their nonlinear form through the full nonlinear equations of motion implemented in the stitched model.

4) The fourth distinction of the stitched model is its ability to scale the forces and moments for changes in mass, moments of inertia, and CG location through the equations of motion, thus allowing for simulation of changes in those parameters without explicitly including them as scheduling parameters. This is an important aspect of the stitched model for use with flight data, which will be discussed further in Section II.C.3.

5) The final distinction of the stitched model is the ability to simulate takeoff and landing through the inclusion of simple landing gear and spoilers models, an engine out condition, and different levels of wind and

turbulence. The resulting model is accurate for typical aircraft flight dynamics for the entire maneuvering flight regime, except for extreme conditions (e.g., stall or spin).

A block diagram schematic of the stitched model is shown in Figure 1 (duplicated from Ref. 3). Note that in this schematic, $\boldsymbol{\rho} = U$, and the model is only stitched with x-body axis velocity U. To summarize, model stitching is accomplished by implementing lookup tables of the aircraft state trim values, control input trim values, and stability and control derivatives based on point models and trim data. Trim states and controls are used to determine perturbation states $[\Delta \boldsymbol{x} = (\boldsymbol{X} - \boldsymbol{X}_0(U))]$ and controls $[\Delta \boldsymbol{u} = (\boldsymbol{U} - \boldsymbol{U}_0(U))]$, which in turn are multiplied by the stability and control derivatives and mass matrix ($\boldsymbol{\mathcal{M}}\boldsymbol{A}\Delta\boldsymbol{u}$ and $\boldsymbol{\mathcal{M}}\boldsymbol{B}\Delta\boldsymbol{x}$) to determine perturbation aerodynamic and control forces and moments. Note that the stability and control derivatives are determined based on a low-pass filtered U_f, to ensure that the derivative values remain constant for short-term motion and retain the accurate dynamic response at the discrete point models. Trim values are determined based on instantaneous U. The aerodynamic trim forces and moments are then summed to the perturbation values to yield the total aerodynamic forces and moments acting on the aircraft in body axes. In addition, the linearized Coriolis terms (e.g., $W_0 q$, etc., due to formulating equations of motion in body axes) and linearized gravity terms normally included in the $\boldsymbol{A}$ and $\boldsymbol{B}$ state-space matrices are removed and added downstream in their nonlinear form.

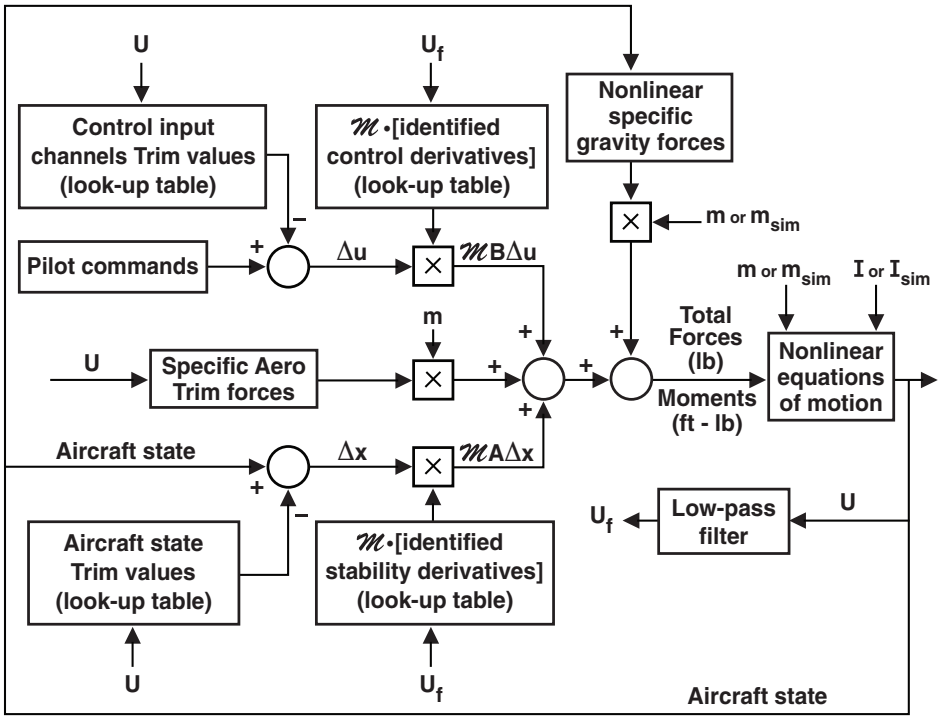

Variable	Description
U	Total longitudinal body axis velocity
U_f	Filtered velocity
$\triangle u$	Control perturbations (e.g., δ_e)
$\triangle x$	State perturbations [e.g., $w \equiv (W - W_0)$]
$\mathcal{M}$	Mass matrix to include a/c mass and inertia
A	Dimensional stability derivatives
B	Dimensional control derivatives
m	Aircraft mass
I	Aircraft inertia matrix

Figure 1. Model stitching block diagram schematic (duplicated from Ref. 3).

C. Development From Flight Data

The linear point models and trim data that go into a stitched model can come from several different sources, including trimming and linearizing high-fidelity nonlinear simulation models that cannot be run in real-time[2,9] or from flight data. One requirement for the linear point models and trim data is that they vary only with the scheduling parameter vector $\boldsymbol{\rho}$, meaning that variations due to other sources (e.g., loading configuration) should be minimized. This is easy to enforce when developing a stitched model from a nonlinear simulation model, for example. However, when developing a stitched model from flight data, it can be impracticable or even impossible to identify all models and collect all trim data at the same loading configuration. Therefore, when developing a stitched model from flight data, care must be taken in designing the flight test, and a pre-processing step is taken which uses the stitched model's capability to scale for changes in weight, CG, and inertia, to "*baseline*" all identified models to a common loading configuration. The following sections will summarize the work flow of creating a stitched model from flight data.

1. Design the Flight Test

The first step in developing a stitched model from flight data is to determine what maneuvers to fly and at what flight conditions. For the recommended frequency-domain identification approach[3] used herein, the primary set of flight data collected are frequency sweeps in each of the control axes at each of the identification flight conditions. Note that where sweeps are not practical (e.g., for identifying the thrust response) pulses, doublets, 3-2-1-1, or other maneuvers may be used. Equally important to the frequency sweep data are the longitudinal speed stability (LSS) data[10] that should be collected around each identification flight condition. These LSS data will have two important uses described later on. Next, steady-heading sideslip data[10] should be collected at each identification flight condition. Validation data in the form of pulses, doublets, or steps in each control axis should also be collected. Finally, "trim shot" data should be collected at each identification altitude that sufficiently spans the airspeed range of the flight conditions to be identified. The trim shot data are collected by trimming the aircraft at the low end of the airspeed range at the appropriate altitude. Then, airspeed is increased with throttle while maintaining a constant altitude until the upper end of the airspeed range, with 10 sec of trim data collected at every 20 kts.

It is important to disable any autotrim functions during these maneuvers, or ensure that their effects can be removed from the data in post processing. For example, for a fixed-wing aircraft with an all-moving stabilator (such as the LJ-25), it is necessary to know the effectiveness of the stabilator as compared to the elevator ($\Delta\delta_\mathrm{e}/\Delta\delta_\mathrm{s}$) in order to correct all elevator data to a common stabilator position. This can be done using a "mis-trim" maneuver, in which the aircraft is trimmed at a given flight condition and stabilator and elevator positions are recorded (δ_{s_1} and δ_{e_1}, respectively). Then, the stabilator is moved to a new position δ_{s_2}, and elevator is used to retrim the aircraft to the original flight condition. The new stabilator and elevator positions are recorded (δ_{s_2} and δ_{e_2}, respectively), and together with the original positions, can be used to determine the effectiveness of the stabilator as compared to the elevator:

$$\frac{\Delta\delta_\mathrm{e}}{\Delta\delta_\mathrm{s}} = \frac{(\delta_{\mathrm{e}_1} - \delta_{\mathrm{e}_2})}{(\delta_{\mathrm{s}_1} - \delta_{\mathrm{s}_2})} \tag{17}$$

This effectiveness ratio can then be used to correct all measured elevator deflections $\delta_{\mathrm{e}_\mathrm{m}}$ to a common stabilator position δ_{s_0}:

$$\delta_{\mathrm{e}_\mathrm{corr}} = \delta_{\mathrm{e}_\mathrm{m}} \frac{\Delta\delta_\mathrm{e}}{\Delta\delta_\mathrm{s}} (\delta_{\mathrm{s}_0} - \delta_{\mathrm{s}_\mathrm{m}}) \tag{18}$$

Tobias and Tischler[2] provide excellent guidance in selecting the airspeed and altitude spacing of the identification flight conditions. Section III lists the flight test conditions and maneuvers flown for the LJ-25. At the end of this step, a database of flight data collected at different flight conditions and loading configurations exists.

2. Identify the Point Models

The second step in developing a stitched model from flight data is identifying the individual point models at each of the identification flight conditions. As mentioned, a frequency-domain identification approach[3]

is the preferred method and the one used herein. This is a two step approach in which first, frequency responses are extracted from the frequency sweep time history flight data. Then, state-space models are fit to the frequency responses and verified in the time domain. These state-space models are the point models (sometimes referred to as "point ID models" when identified from flight data) used to build up the stability and control derivative lookup tables in the stitched model. An example identification of the longitudinal axis dynamics at one flight condition is shown for the LJ-25 in Section IV.

In general, it is difficult to identify the long-period aircraft dynamics (e.g., phugoid mode), as getting good frequency response data at those low frequencies requires long time history record lengths.[3] Lack of low-frequency data can make the speed derivatives of the identified state-space models (i.e., X_u, Z_u, and M_u) insensitive and not well determined. Therefore, the LSS data is used to determine and fix these derivatives in the identification process.[3] This process is demonstrated for the LJ-25 in Section IV.B.3.

Steady heading sideslip data can be used to check or determine and fix the lateral speed derivatives[3] (i.e., Y_v, L_v, and N_v). Finally, the accuracy of the individual point models is verified in the time domain using the validation data. This is shown for the LJ-25 in Section IV.B.5. At the end of this step, a database of point ID models and LSS data at different flight conditions and loading configurations exists.

3. Baseline the Point Models and Longitudinal Speed Stability Data

The third step in developing a stitched model from flight data is to take the individual point ID models and LSS data and scale, or *baseline*, them to one common loading configuration—the *stitched model loading configuration*. This is done by simply setting m_{sim} and I_{sim} in Figure 1 to the stitched model loading configuration values. Recall that this is a necessary step since the linear point models and trim data that go into the stitched model should only vary with the scheduling parameter (airspeed and flap deflection in the case of the LJ-25 application).

Baselining the point models and LSS data is an important step for conventional aircraft, where fuel burn during the flight test means that data collected for model identification at the beginning of the flight corresponded to one loading configuration, while data collected at the end of the flight to a different loading configuration. For an electric propulsion aircraft for example, this step could be skipped, since energy consumption from the battery during the flight does not change the aircraft loading configuration.

This step is accomplished using the stitched model. The stitched model is populated with a single point ID model and that model's corresponding LSS data. Recall that LSS data is taken at constant thrust (or throttle) but varying altitude (flight path angle $\gamma \neq 0$). In general, the trim data used in the stitched model is of constant altitude ($\gamma = 0$) but varying thrust (trim shot data). Therefore, in addition to using this step to baseline each point ID model to the common stitched model loading configuration, this step is also used to baseline and *repurpose* the LSS data into trim shot data. This is accomplished by trimming the single point ID model in the stitched model at airspeeds around its trim condition with varying thrust, but constant altitude. This produces a more finely spaced set of constant altitude trim data around each point ID model, that can be used to supplement the trim shot data. The details of the model baselining and LSS data repurposing are shown for the LJ-25 in Sections V and VI. At the end of this step, a new database of point ID models and finely spaced trim data at different flight conditions, but all at the common stitched model loading configuration exists.

4. Combine the Point Models and Trim Data and Populate the Stitched Model

The fourth and final step in developing a stitched model from flight data is to combine the baselined point ID models, along with the trim data, and populate the stitched model lookup tables. Here, certain trends in the trim data, or in the stability and control derivatives, can be checked or enforced by fitting linear or quadratic least squares fits to the data. These fits can be used to interpolate yet finer grids of trim data, or to extrapolate data beyond the edges of the identification envelope. The LJ-25 data is presented in Section VII.

III. Flight Test Overview

The primary objective of the flight test described in this paper was to collect a database of system identification flight data on the Learjet at various flight and loading conditions, including piloted frequency sweeps, doublets, trim data, longitudinal speed stability, and steady-heading sideslips. The remainder of this section will give a description of the aircraft and the test points flown.

A. Aircraft Description

The aircraft used in this study is the Calspan Variable Stability System (VSS) Learjet LJ-25D, shown in Figure 2. It is a twin turbojet-powered business jet which in its unmodified state can carry eight passengers. It has a maximum take-off weight (MTOW) of 15,000 lbs, a cruise speed of 464 KTAS, a maximum range of 1,535 nm, and a service ceiling of 45,000 ft.

The aircraft is instrumented with sensors to measure air data (α, β, V_{tot}, $\bar{q}$, $\dot{h}$, and outside air temperature), aircraft states (ϕ, θ, ψ, p, q, r, n_x, n_y, and n_z), controls (pilot stick and pedal force $F_{\text{lat,lon,ped}}$ and positions $\delta_{\text{lat,lon,ped}}$, surface deflections $\delta_{\text{a,e,r}}$, engine fuel control, and derived engine thrust δ_{T}), GPS measurements, and INS (H-423 Ring Laser Gyro).

Figure 2. Calspan Variable Stability System Learjet LJ-25D.

B. Test Points

Table 1 lists the flight condition and maneuvers flown at each test point. The test points are plotted against the LJ-25 flight envelope in Figure 3. Note that the points cover only a small portion of the envelope, but produce sufficient data to develop a full-envelope stitched model of this aircraft. For this test, the majority of the data were collected at 15,000 ft. This is a relatively low altitude compared to the flight envelope (Figure 3), however, was selected because is it the primary altitude at which the USAF TPS operates the Learjet.

Model identification data consisted of piloted frequency sweeps in the longitudinal, lateral, and directional axes, thrust doublets, longitudinal speed stability data, and steady heading sideslip data flown at five conditions for model development (Points 1 through 5, Table 1) and two conditions for model validation (Points 7 and 8, Table 1). Piloted frequency sweeps were used in favor of automated frequency sweeps because of their richer frequency content and improved ability to keep the aircraft on trim condition.

Trim data were collected at airspeeds spanning the identification points (185–300 kts) at increments of approximately 20 kts in one trim shot maneuver (Point 6, Table 1). Additional validation data consisting of piloted doublets in the longitudinal, lateral, and directional axes were collected at Points 9 and 10, Table 1.

Note that Points 1 and 2 (Table 1, Figure 3) were repeated at the same flight condition (185 kts, 15,000 ft), but Point 1 is a powered approach configuration (gear down, flaps 20), while Point 2 is a clean configuration. Identifying these two models at the same flight condition allowed determining flap and gear effects on the stability and control derivatives and trim data.

Two models were also identified at the 250 kts, 15,000 ft flight condition (Points 4 and 7, Table 1, Figure 3). Point 4 was flown in a light loading configuration (with the tip fuel tanks empty) and the model identified from the data at this point was used in the development of the stitched model. Point 7, on the other hand, was flown in a heavy loading configuration (with the tip fuel tanks full) and the model identified from the data at this point was used to validate the stitched model's capability to scale for loading configuration (as shown in Section V).

Additional validation flight data were gathered as part of a follow-on flight test.[11] Although those points are not shown in Table 1 or Figure 3, some of those results are presented in Section VIII.

Table 1. Test Matrix of Flight Conditions and Maneuvers Flown

Point	Speed [KIAS]	Altitude [ft]	Gear/ Flaps	Trim Shot	Piloted Sweeps[a]	Doublets[b]	Speed Stability	Steady Sideslips
Model Development Data								
1	185	15000	DN/20	-	✓	✓	✓	✓
2	185	15000	UP/UP	-	✓	✓	✓	✓
3	220	15000	UP/UP	-	✓	✓	✓	✓
4	250	15000	UP/UP	-	✓	✓	✓	✓
5	300	15000	UP/UP	-	✓	✓	✓	✓
6	185–300	15000	UP/UP	✓	-	-	-	-
Model Validation Data								
7	250	15000	UP/UP	-	✓	✓	✓	✓
8	275	15000	UP/UP	-	✓	✓	✓	✓
9	140	10000	DN/20	-	-	✓	-	-
10	135	6000	DN/20	-	-	✓	-	-

[a] Frequency sweeps in pitch, roll, and yaw
[b] Doublets in pitch, roll, yaw, and throttle

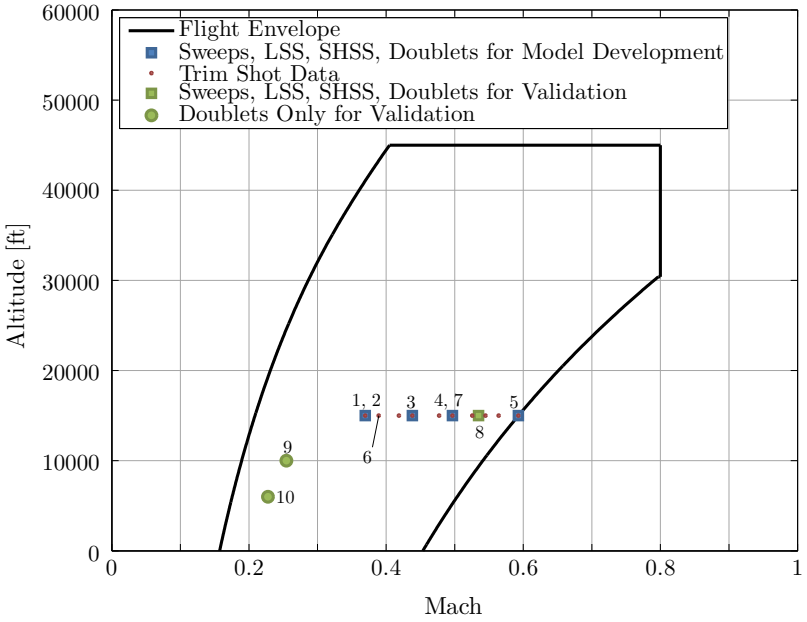

Figure 3. Learjet-25 flight envelope with flight test points.

IV. Point Model Identification

Longitudinal and lateral/directional state-space models were identified at seven of the test points—Points 1, 2, 3, 4, 5, 7, and 8 (Table 1, Figure 3). As mentioned in Section III.B, five of these models were used to develop the stitched model, while the remaining two were only used for validation. Frequency domain identification was done in two steps using the CIFER® software tool.[3] First, frequency responses of the aircraft outputs were extracted from the frequency sweep flight data. Next, state-space models were fit to the frequency response data. The following sections will provide the forms of the state-space models used, and show example identification results for one flight condition.

A. Identification Model Form

The identified longitudinal and lateral/directional models are represented in state-space form:

$$\begin{aligned} \dot{\boldsymbol{x}} &= \boldsymbol{A}\boldsymbol{x} + \boldsymbol{B}\boldsymbol{u} \\ \boldsymbol{y} &= \boldsymbol{C}\boldsymbol{x} + \boldsymbol{D}\boldsymbol{u} \end{aligned} \tag{19}$$

The models are in body axes, and have the forms given in Equation 20 and Equation 21, respectively.

$$\begin{bmatrix} \dot{u} \\ \dot{w} \\ \dot{q} \\ \dot{\theta} \end{bmatrix} = \begin{bmatrix} X_u & X_w & X_q - W_0 & -g\cos\Theta_0 \\ Z_u & Z_w & Z_q + U_0 & -g\sin\Theta_0 \\ M_u & M_w & M_q & 0 \\ 0 & 0 & 1 & 0 \end{bmatrix} \begin{bmatrix} u \\ w \\ q \\ \theta \end{bmatrix} + \begin{bmatrix} X_{\delta_\mathrm{e}} & X_{\delta_\mathrm{T}} \\ Z_{\delta_\mathrm{e}} & Z_{\delta_\mathrm{T}} \\ M_{\delta_\mathrm{e}} & M_{\delta_\mathrm{T}} \\ 0 & 0 \end{bmatrix} \begin{bmatrix} \delta_\mathrm{e} \\ \delta_\mathrm{T} \end{bmatrix}$$

$$\begin{bmatrix} q \\ \alpha \\ a_x \\ a_z \\ \dot{u} \\ \dot{w} \end{bmatrix} = \begin{bmatrix} 0 & 0 & 1 & 0 \\ 0 & 1/U_0 & 0 & 0 \\ X_u & X_w & X_q & 0 \\ Z_u & Z_w & Z_q & 0 \\ X_u & X_w & X_q - W_0 & -g\cos\Theta_0 \\ Z_u & Z_w & Z_q + U_0 & -g\sin\Theta_0 \end{bmatrix} \begin{bmatrix} u \\ w \\ q \\ \theta \end{bmatrix} + \begin{bmatrix} 0 & 0 \\ 0 & 0 \\ X_{\delta_\mathrm{e}} & X_{\delta_\mathrm{T}} \\ Z_{\delta_\mathrm{e}} & Z_{\delta_\mathrm{T}} \\ X_{\delta_\mathrm{e}} & X_{\delta_\mathrm{T}} \\ Z_{\delta_\mathrm{e}} & Z_{\delta_\mathrm{T}} \end{bmatrix} \begin{bmatrix} \delta_\mathrm{e} \\ \delta_\mathrm{T} \end{bmatrix} \tag{20}$$

$$\begin{bmatrix} \dot{v} \\ \dot{p} \\ \dot{r} \\ \dot{\phi} \end{bmatrix} = \begin{bmatrix} Y_v & Y_p + W_0 & Y_r - U_0 & g\cos\Theta_0 \\ L_v & L_p & L_r & 0 \\ N_v & N_p & N_r & 0 \\ 0 & 1 & \tan\Theta_0 & 0 \end{bmatrix} \begin{bmatrix} v \\ p \\ r \\ \phi \end{bmatrix} + \begin{bmatrix} Y_{\delta_\mathrm{a}} & Y_{\delta_\mathrm{r}} \\ L_{\delta_\mathrm{a}} & L_{\delta_\mathrm{r}} \\ N_{\delta_\mathrm{a}} & N_{\delta_\mathrm{r}} \\ 0 & 0 \end{bmatrix} \begin{bmatrix} \delta_\mathrm{a} \\ \delta_\mathrm{r} \end{bmatrix}$$

$$\begin{bmatrix} p \\ r \\ a_y \\ \beta \\ \dot{v} \end{bmatrix} = \begin{bmatrix} 0 & 1 & 0 & 0 \\ 0 & 0 & 1 & 0 \\ Y_v & Y_p & Y_r & 0 \\ 1/V_\mathrm{tot} & 0 & 0 & 0 \\ Y_v & Y_p + W_0 & Y_r - U_0 & g\cos\Theta_0 \end{bmatrix} \begin{bmatrix} v \\ p \\ r \\ \phi \end{bmatrix} + \begin{bmatrix} 0 & 0 \\ 0 & 0 \\ Y_{\delta_\mathrm{a}} & Y_{\delta_\mathrm{r}} \\ 0 & 0 \\ Y_{\delta_\mathrm{a}} & Y_{\delta_\mathrm{r}} \end{bmatrix} \begin{bmatrix} \delta_\mathrm{a} \\ \delta_\mathrm{r} \end{bmatrix} \tag{21}$$

The derivatives of body velocities ($\dot{u}$, $\dot{v}$, and $\dot{w}$) were reconstructed from inertial measurements[3] for use in the model identification:

$$\dot{u} = a_x - W_0 q + V_0 r - (g\cos\Theta_0)\theta \tag{22}$$

$$\dot{v} = a_y - U_0 r + W_0 p + (g\cos\Theta_0)\phi \tag{23}$$

$$\dot{w} = a_z - V_0 p + U_0 q - (g\sin\Theta_0)\theta \tag{24}$$

B. Results

Example identification results are presented here for the Point 4 (250 kts, 15,000 ft, light weight configuration) longitudinal model. First, the frequency responses extracted from the frequency sweep flight test data will be provided. Then, an analysis of the LSS data will be provided. Finally, the results of the state-space model identification will be provided.

1. Time Histories

An example longitudinal axis frequency sweep is shown in Figure 4. In general, two sweeps were repeated in each axis at each flight condition. The frequency sweeps began with about 5 sec of trim data, followed by two 20-sec period oscillations ($\omega \approx 0.3$ rad/sec), and then a frequency progression up to about 2 Hz

($\omega \approx 12.6$ rad/sec). Sweep record lengths T_{rec} were determined based on the expected modes of interest [$T_{\text{rec}} = 11/(\zeta\omega)$], especially important for capturing the lightly damped Dutch roll mode.

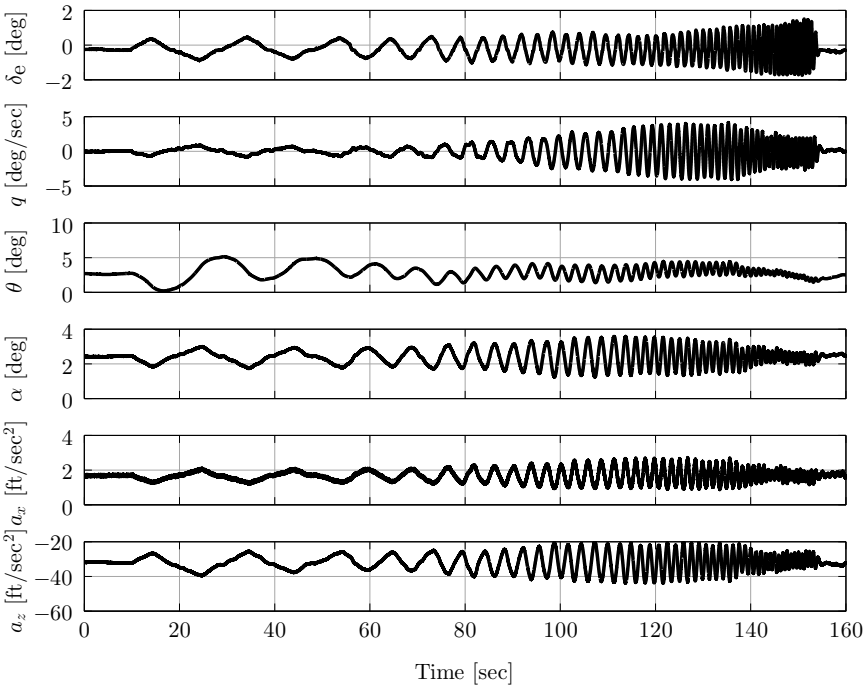

Figure 4. Example longitudinal axis frequency sweep time history (250 kts, 15,000 ft, light weight configuration).

2. *Frequency Responses*

Figures 5 through 10 show the longitudinal axis frequency responses that were extracted from the pitch frequency sweeps for Point 4. Indicated on the figures are the frequency ranges of each response used in the state-space model identification (solid black part of the frequency responses), based on the region of good coherence ($\gamma \geq 0.6$).[3] Overall, the data show exceptionally high coherence for all responses, very smooth frequency response identification, and clear presence of classic models such as the short-period at $\omega \approx 4$ rad/sec.

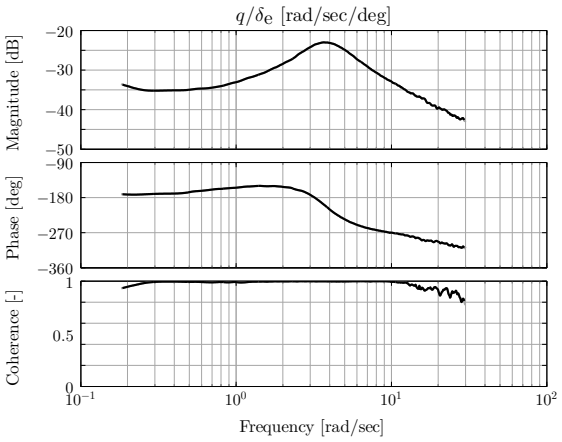

Figure 5. Pitch rate frequency response (250 kts, 15,000 ft, light weight configuration).

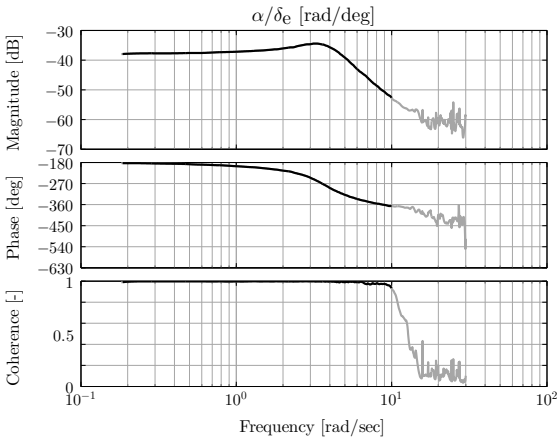

Figure 6. Angle of attack frequency response (250 kts, 15,000 ft, light weight configuration).

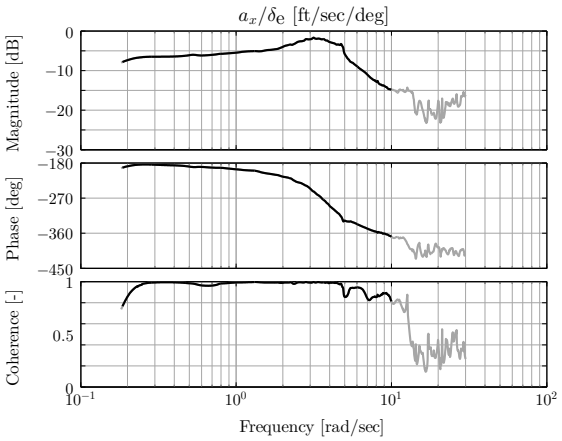

Figure 7. Longitudinal acceleration frequency response (250 kts, 15,000 ft, light weight configuration).

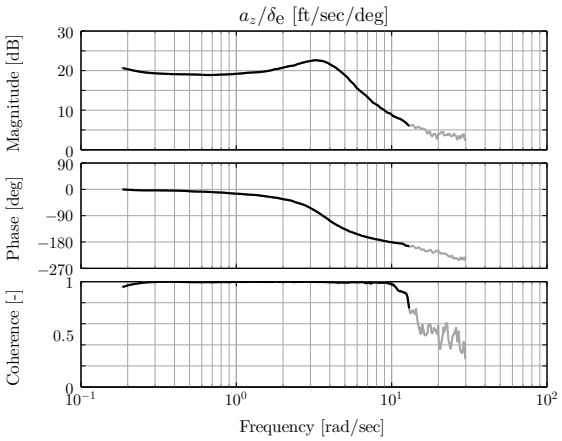

Figure 8. Vertical acceleration frequency response (250 kts, 15,000 ft, light weight configuration).

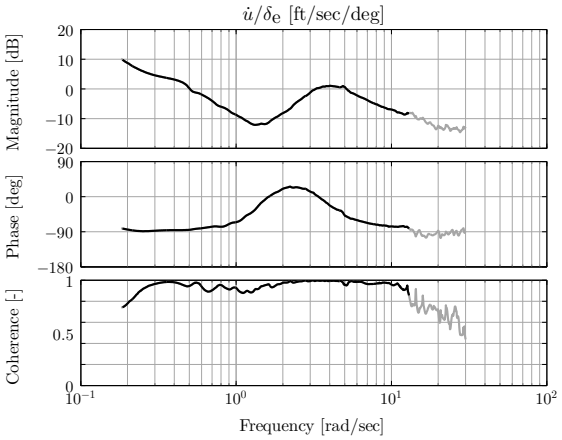

Figure 9. Derivative of x-axis body velocity frequency response (250 kts, 15,000 ft, light weight configuration).

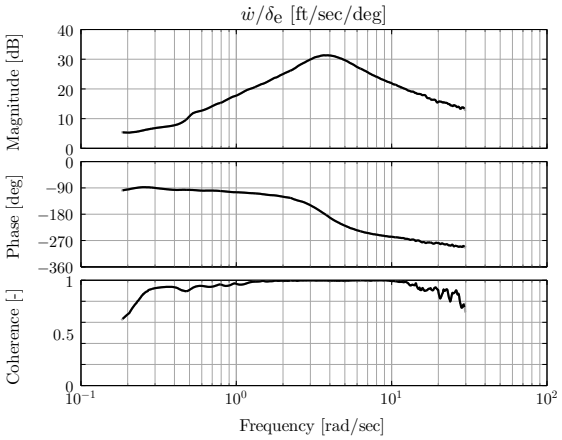

Figure 10. Derivative of z-axis body velocity frequency response (250 kts, 15,000 ft, light weight configuration).

3. Longitudinal Speed Stability Data

In addition to the frequency sweep data gathered for model identification and doublet data gathered for model validation, longitudinal speed stability (LSS) data were gathered using the stabilized point technique.[12] The aircraft was trimmed around the identification point flight condition (250 kts, 15,000 ft in this case), throttle position was held constant, and airspeed was varied by climbing and descending. Airspeed was stabilized at three points above and three points below the trim condition (approximately 10 kts apart).

Figure 11 shows the full maneuver time history. Highlighted in red on the time history data are sections where the airspeed was stabilized, and the aircraft was in trim. Trim pitch attitude θ, z-body axis velocity $W = V_{\text{tot}} \sin\alpha$, elevator deflection δ_e, and estimated thrust δ_T were averaged over each of the highlight sections and then plotted against x-body axis velocity $U = V_{\text{tot}} \cos\alpha$ to determine the trim gradients (as shown in Figure 12). These trim gradients were used to determine and fix the u-stability derivatives (i.e., X_u, Z_u, and M_u) in the state-space model identification. This is done by recognizing that in trim $\dot{u} = 0$. Then, the state-space equations can be used to solve for the u-stability derivatives as a function of the other derivatives and the trim gradients, as is shown here for the X_u derivative:[3]

$$\Delta\dot{u} = X_u\Delta u + X_w\Delta w + (X_q - W_0)\Delta q - g\cos\Theta_0\Delta\theta + X_{\delta_e}\Delta\delta_e \quad (25)$$

$$X_u = -X_w\frac{\Delta w}{\Delta u} + g\cos\Theta_0\frac{\Delta\theta}{\Delta u} - X_{\delta_e}\frac{\Delta\delta_e}{\Delta u} \quad (26)$$

Note that the $X_{\delta_T}\Delta\delta_T$ term is eliminated from Equation 25, because the LSS data is taken at constant throttle, and therefore $\Delta\delta_T$ is assumed to be 0 (which is seen to nearly be the case in the bottom plot in Figure 11).

For the data presented in Figure 12, X_u is calculated to be (Equation 26):

$$\begin{aligned} X_u &= -(0.0857)(-0.0934) + (32.146)(-0.000483) - (0.0727)(0.0127) \\ &= 0.0080 - 0.0155 - 0.000923 \\ &= -0.0084 \end{aligned} \quad (27)$$

with the main contributions coming from the $(g\cos\Theta_0)(\Delta\theta/\Delta u)$ and $(X_w)(\Delta w/\Delta u)$ terms.

This process of determining and fixing the u-stability derivatives is an iterative one, as it requires knowing the values of the other derivatives first. That, in turn, requires identifying the state-space model before fixing the u-stability derivatives. Once the u-stability derivatives are fixed, the remaining derivatives are re-identified. Experience indicates that the values change very little, due to the frequency separation between the phugoid and short-period modes, and that additional iterations of this process are not needed.

As described in Section II.C.2 and Ref. 3, this method of fixing the u-stability derivatives is preferred to freeing them in the state-space identification process since there is typically no frequency responses data at frequencies low enough to capture the phugoid dynamics. Therefore, freeing the u-stability derivatives would result in large insensitivity values for those derivatives. This also ensures that the speed derivatives will be consistent with the stitched model implementation. For example, X_u from Equation 26 and $X_{u_{\text{qLPV}}}$ from Equation 12 will be equal if the trim and control gradients used to determine X_u are the same as those used in the stitched model. This will be shown in Section VI.

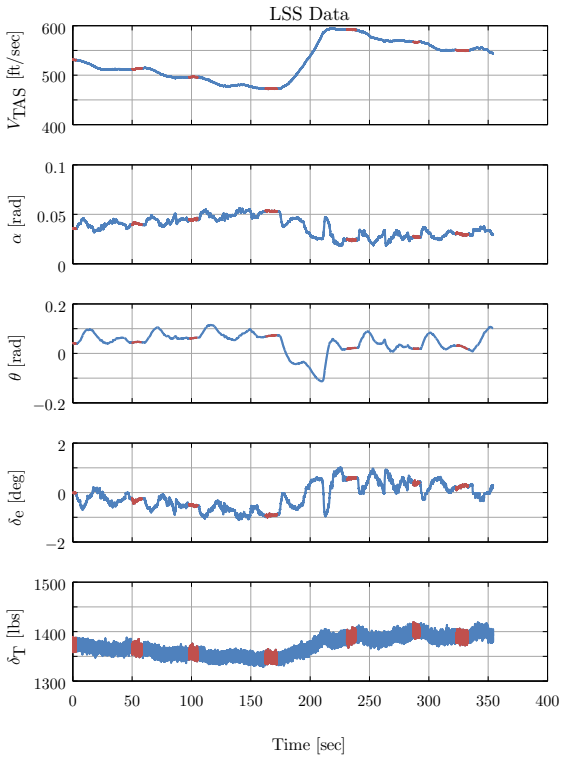

Figure 11. Longitudinal speed stability maneuver time history (250 kts, 15,000 ft, light weight configuration).

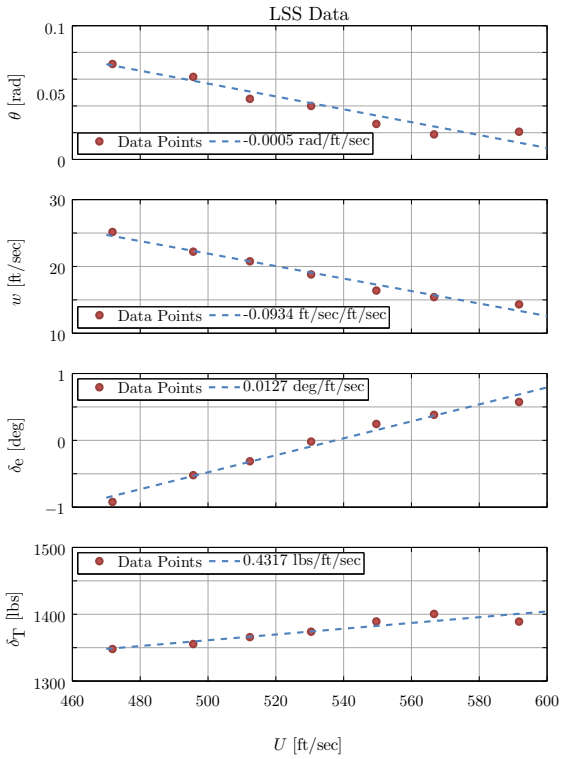

Figure 12. Trim gradients extracted from longitudinal speed stability maneuver time history (250 kts, 15,000 ft, light weight configuration).

4. *State-Space Model Identification*

The state-space model form given in Equation 20 was fit to the frequency responses shown in Figures 5 through 10 using the DERIVID tool in CIFER®.[3] The identification results are shown in Figures 13 through 18. The individual and average fit cost values are given in Table 2. The costs are calculated as a weighted sum of the magnitude and phase errors between the frequency responses and the model responses.[3] The figures show an excellent model fit, which is confirmed by the low individual and average fit costs given in Table 2 (costs of $J < 50$ indicate near perfect agreement[3]).

The identified parameter values as well as their insensitivity and Cramér-Rao bounds are given in Table 3. All identified parameters are *known to good accuracy* and not correlated with any other parameters as indicated by their low insensitivity ($\bar{\text{I}} \leq 10\%$[3]) and Cramér-Rao bound ($\overline{\text{CR}} \leq 20\%$[3]) values.

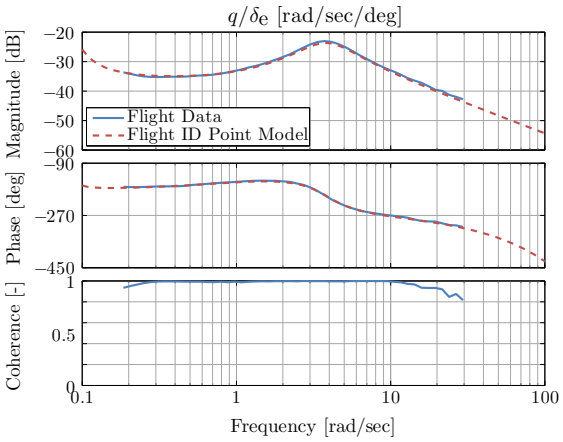

Figure 13. Pitch rate model fit (250 kts, 15,000 ft, light weight configuration).

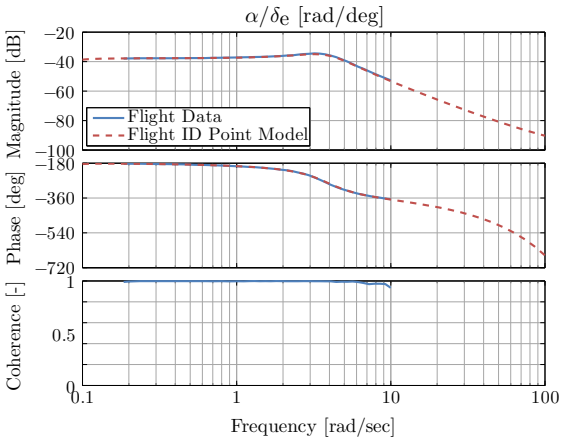

Figure 14. Angle of attack model fit (250 kts, 15,000 ft, light weight configuration).

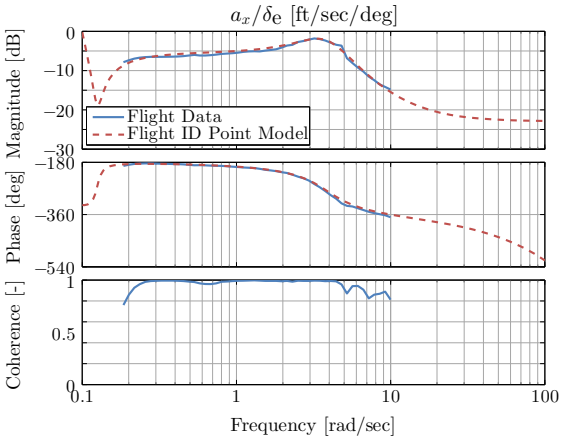

Figure 15. Longitudinal acceleration model fit (250 kts, 15,000 ft, light weight configuration).

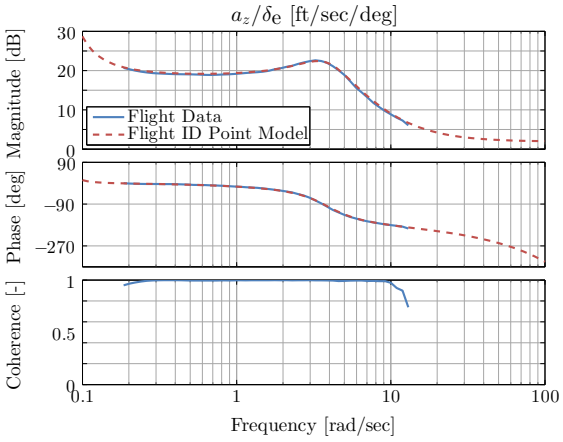

Figure 16. Vertical acceleration model fit (250 kts, 15,000 ft, light weight configuration).

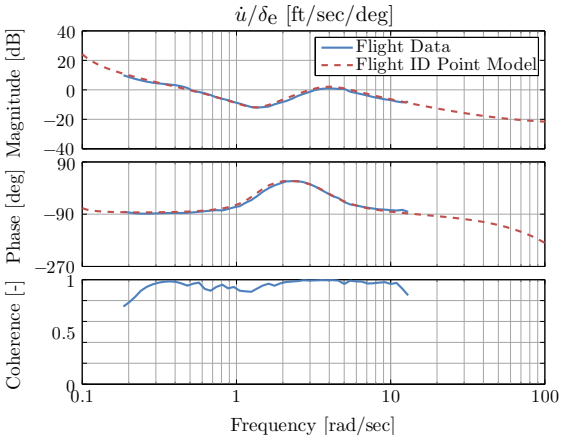

Figure 17. Derivative of x-axis body velocity model fit (250 kts, 15,000 ft, light weight configuration).

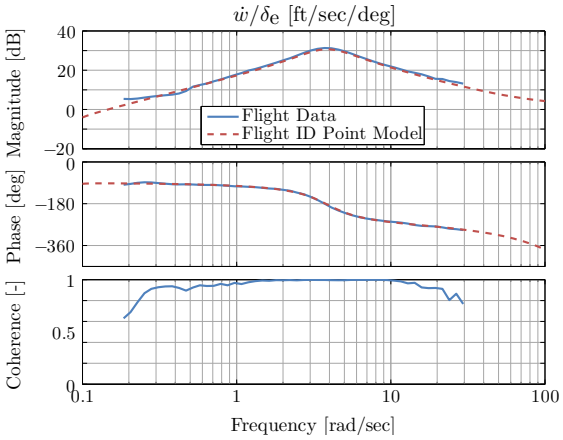

Figure 18. Derivative of z-axis body velocity model fit (250 kts, 15,000 ft, light weight configuration).

Table 2. State-Space Model Identification Fit Costs (250 kts, 15,000 ft, light weight configuration)

Response	Cost (J)
α/δ_e	1.327
q/δ_e	5.145
a_x/δ_e	9.048
a_z/δ_e	1.492
$\dot{u}/\delta_e$	25.11
$\dot{w}/\delta_e$	14.07
J_{ave}	9.366

Table 3. State-Space Model Identification Parameter Values (250 kts, 15,000 ft, light weight configuration)

Param.	Value	CR (%)	Insens. (%)
	A-matrix		
X_u	-0.008429[a]	–	–
X_w	0.08624	3.572	1.239
X_q	0[b]	–	–
Z_u	-0.1241[a]	–	–
Z_w	-1.43	3.289	1.153
Z_q	0[b]	–	–
M_u	0.000237[a]	–	–
M_w	-0.02351	2.815	0.9107
M_q	-1.652	9.445	2.727
	B-matrix		
X_{δ_e}	0.07138	23.66	9.218
Z_{δ_e}	-1.249	17.78	6.881
M_{δ_e}	-0.192	2.976	0.7492
	Time delay		
τ_E	0.02771	11.13	5.169
τ_V	0.0607	19.94	9.59

[a] Fixed parameter
[b] Eliminated parameter

This process of extracting frequency responses from the flight data and identifying a model was repeated to add the thrust control derivatives (X_{δ_T}, Z_{δ_T}, and M_{δ_T}) to the longitudinal model and to identify the lateral/directional models at each flight condition.

5. *Time Domain Validation*

After identification of the state-space model, piloted doublet flight data (that was not used for identification) was used to verify the results in the time domain. Figure 19 shows the elevator input from flight data that was used to simulate the identified state-space model, as well as the comparison of the flight and model outputs.

The model captures the dynamics of the Learjet very well, which is shown by the excellent agreement of the flight and model data in the figures, as well as by the low RMS fit error cost ($J_{\text{RMS}} = 0.47$ for the maneuver shown). Values of $J_{\text{RMS}} \leq 1.0$ reflect a good level of accuracy.[3]

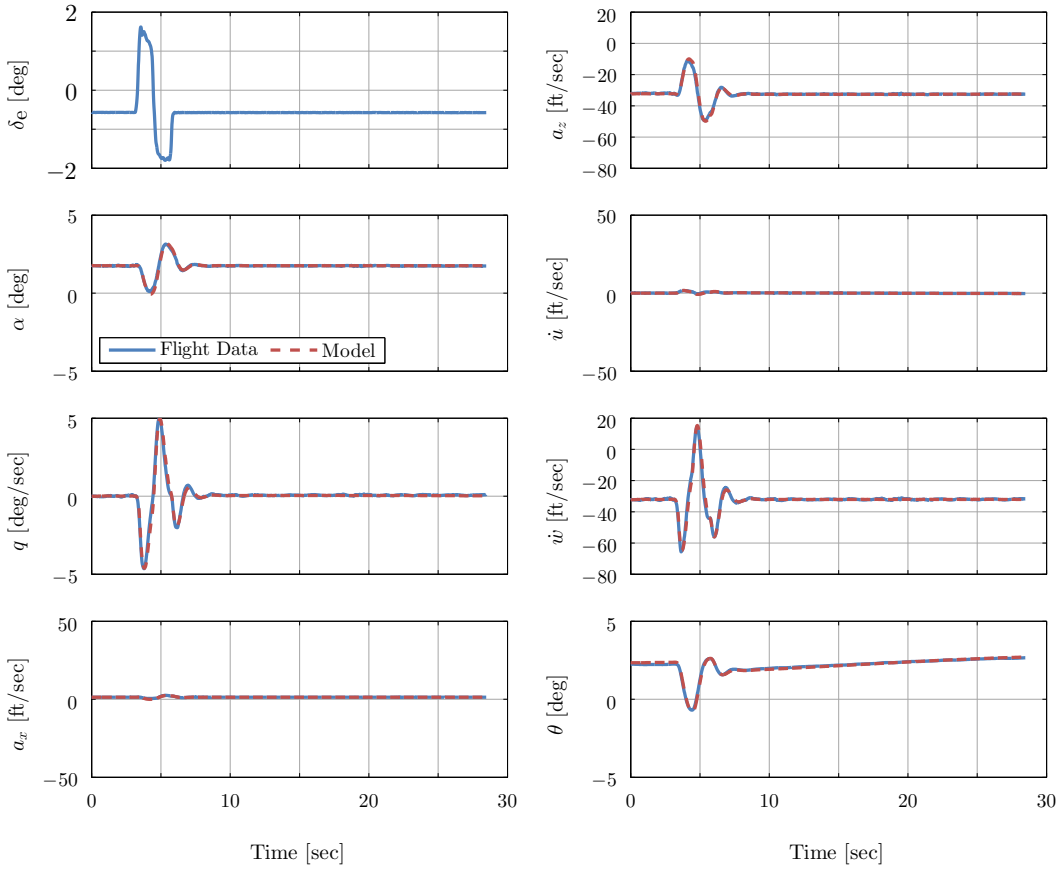

Figure 19. Time domain verification results (250 kts, 15,000 ft, light weight configuration).

Once the process laid out in Sections IV.B.1 to IV.B.5 was completed for the other flight conditions, Step 2 in Section II.C was completed.

V. Model Scaling

After individual point models at each flight condition were identified, the next step was to scale or "baseline" the models to a common loading configuration (Section II.C.3). Recall that this is a necessary step since the stitched model requires all models to be at the same loading configuration. This scaling technique is demonstrated here for the 250 kts flight condition, at which identification was done at two loading configurations, described in Table 4.

First, example identification results will be given for the two loading configurations at the 250 kts, 15,000 ft flight condition:

Configuration 1: Point 4, 250 kts, 15,000 ft, empty tip tanks, light weight, forward X_{cg}
Configuration 2: Point 7, 250 kts, 15,000 ft, full tip tanks, heavy weight, aft X_{cg}

Then, the identification results will be used to determine the moments of inertia of the two configurations, which are needed to scale the stitched model. Finally, using the stitched model's scaling capability, the Configuration 1 model will be scaled to the loading configuration of Configuration 2 and the results will be compared against the Configuration 2 flight identified model.

Table 4. Loading Configurations (250 kts, 15,000 ft)

	Configuration 1 Light/Fwd	Configuration 2 Heavy/Aft
Tip Tank Fuel [lbs]	0	1919.4
Total Fuel [lbs]	2328.6	4580.3
Total Weight [lbs]	12,026.6	14,281.3
X_{cg}[a][ft]	1.29	1.59

[a] Distance along mean aerodynamic chord c; derived parameter from known fuel load

A. Trim and Frequency Response Comparison

Figures 20 through 23 show comparisons of the primary on-axis frequency responses for the two configurations. As expected, the short period mode of Configuration 2 (Heavy/Aft), seen in the pitch rate response in Figure 20, as well as the Dutch roll mode of Configuration 2, seen in the roll rate response in Figure 22 and sideslip response in Figure 23, are at lower frequencies. In addition, the high-frequency asymptotes of the responses of Configuration 2 (Heavy/Aft) are at a lower magnitude as compared to Configuration 1 (Light/Fwd). This is much more noticeable in the roll rate and sideslip responses (Figure 22 and Figure 23, respectively), than in the pitch rate response (Figures 20), suggesting much larger variations in the roll and yaw moments of inertia (I_{xx} and I_{zz}) than pitch moment of inertia (I_{yy}) as expected from the large tip tank fuel load variation between the light and heavy configurations.

A fuel slosh mode can be seen in the pitch rate response (Figure 20) of Configuration 2 (Heavy/Aft) at around $\omega = 20$ rad/sec. Note that this mode is only present when the tip tanks are near full. Therefore, it was not included as part of the identification and so does not show up in the model.

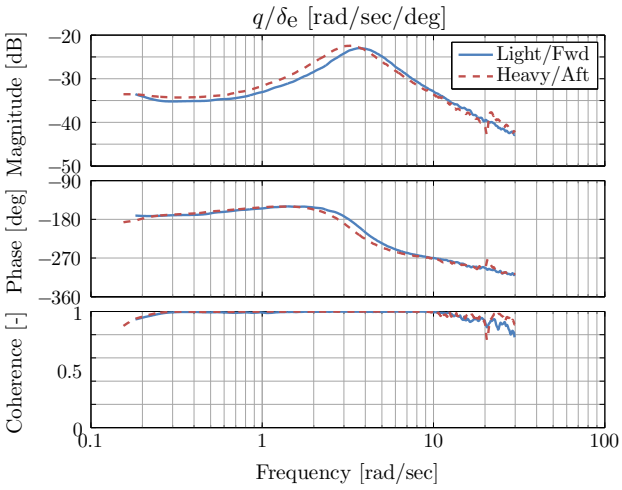

Figure 20. Pitch rate response to elevator input comparison (250 kts, 15,000 ft).

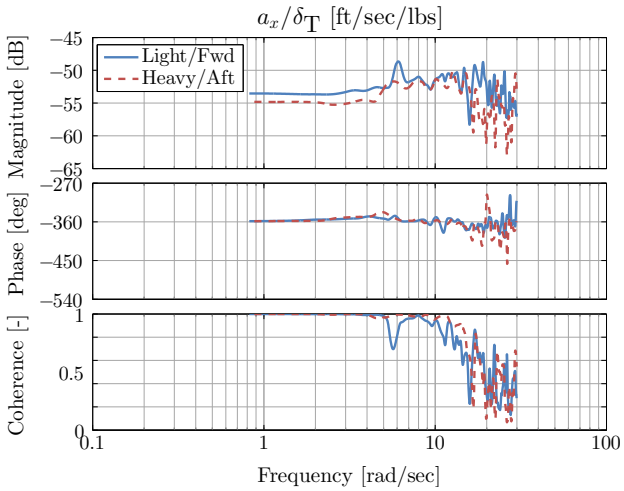

Figure 21. Vertical acceleration response to thrust input comparison (250 kts, 15,000 ft).

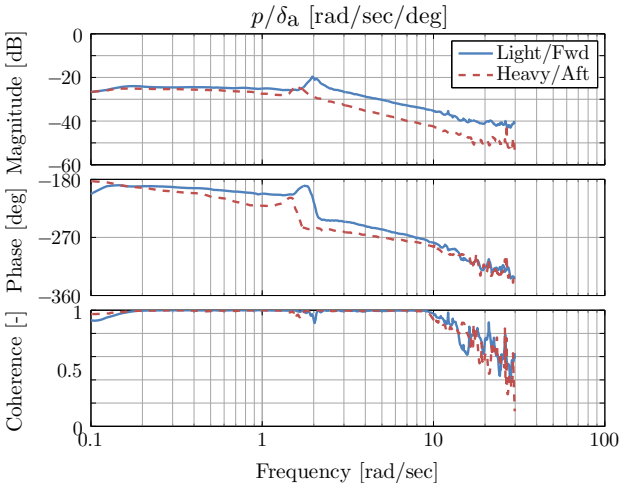

Figure 22. Roll rate response to aileron input comparison (250 kts, 15,000 ft).

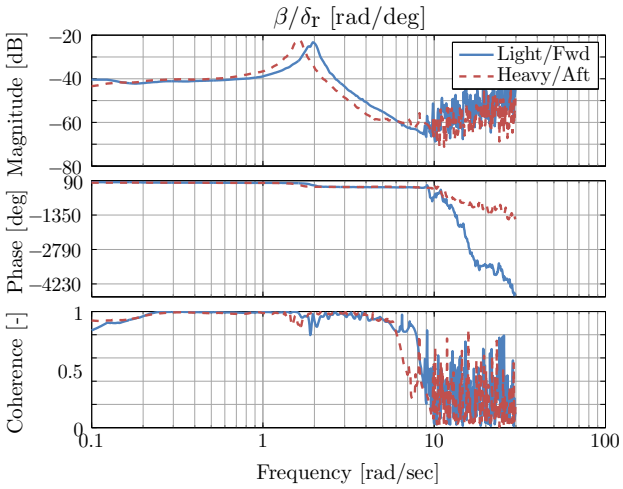

Figure 23. Sideslip response to rudder input comparison (250 kts, 15,000 ft).

Table 5 shows a trim comparison of the two configurations. Note that the ratio of the trim angles of attack of the two configurations ($\alpha_{0_1}/\alpha_{0_2} = 0.83$) matches very closely the ratio of the weights of the two configurations ($W_1/W_2 = 0.84$). This suggests a linear C_{L_α} in this range of angle of attack. Trim elevator deflections δ_{e_0} were corrected to a common stabilator position $\delta_{s_0} = 0$ using Equation 18. It is interesting to note that the heavier configuration is trimmed with a small elevator deflection. At first glance this appears counterintuitive, however, this is due to the fact that the heavier configuration also has a further aft X_{cg} (i.e., smaller static margin). Therefore, the moment that the down force on the tail has to cancel out is actually smaller for the heavy/aft configuration, and a smaller trim elevator deflection is needed.

Tables 6 and 7 show a comparison of the stability and control derivatives between the two loading configurations in the longitudinal and lateral/directional axes, respectively.

Table 5. Trim Values Comparison (250 kts, 15,000 ft)

	Config. 1 Light/Fwd	Config. 2 Heavy/Aft
θ_0 [deg]	2.378	2.882
α_0 [deg]	2.378	2.882
δ_{e_0} [deg]	−4.128	−3.968
δ_{s_0} [deg]	0	0
δ_{T_0} [lbs]	1366.3	1455.9

Table 6. Longitudinal S&C Derivatives Comparison (250 kts, 15,000 ft)

Param.	Config. 1	Config. 2
	A-matrix	
X_u	–0.009725	–0.009896
X_w	0.08642	0.08382
X_q	0	0
Z_u	–0.1119	–0.08969
Z_w	–1.432	–1.142
Z_q	0	0
M_u	0.0004093	0.0008353
M_w	–0.02352	–0.01783
M_q	–1.65	–1.554
	B-matrix	
X_{δ_e}	0.07084	0.07811
X_{δ_T}	0.002289	0.001944
Z_{δ_e}	–1.244	–0.9845
Z_{δ_T}	–0.001053	–0.0009109
M_{δ_e}	–0.1919	–0.1856
M_{δ_T}	–3.826e–05	–3.444e–05

Table 7. Lateral/Directional S&C Derivatives Comparison (250 kts, 15,000 ft)

Param.	Config. 1	Config. 2
	A-matrix	
Y_v	–0.1698	–0.1454
Y_p	0.8673	0.527
Y_r	0	0
L_v	–0.01918	–0.009209
L_p	–2.278	–1.035
L_r	0.8487	0.7406
N_v	0.005268	0.004034
N_p	–0.2258	–0.1004
N_r	–0.2719	–0.1859
	B-matrix	
Y_{δ_a}	–0.0132	–0.02062
Y_{δ_r}	0.3073	0.2368
L_{δ_a}	–0.1623	–0.07185
L_{δ_r}	0.03301	0.0173
N_{δ_a}	–0.01127	–0.003775
N_{δ_r}	–0.03732	–0.02688

B. Moments of Inertia Determination

Moment of inertia estimates were determined from the models of the two configurations. If we assume a constant pitch moment of inertia I_{yy} between the two configurations (as suggested by the similar magnitudes of the high-frequency asymptotes of the pitch rate frequency responses in Figure 20), we can use the ratio of the M_w stability derivative (Table 6) and X_{cg} (Table 4) difference between the two configurations to calculate an average I_{yy}.[3] Recognizing that:[13]

$$M_w = \frac{\rho S U c}{2 I_{yy}} C_{M_\alpha} \tag{28}$$

and:

$$C_{M_\alpha} = C_{L_\alpha} \left(\frac{X_{cg} - X_{np}}{c} \right) \tag{29}$$

the location of the neutral point X_{np} can be determined by solving:

$$\frac{M_{w_2}}{M_{w_1}} = 0.758 = \frac{X_{cg_2} - X_{np}}{X_{cg_1} - X_{np}} \tag{30}$$

The neutral point is calculated to be $X_{np} = 2.53$ ft (or $\bar{X}_{np} = 35.9\%$ MAC). The remaining value needed in order to determine I_{yy} is C_{L_α}, which can be calculated based on:[13]

$$C_{L_\alpha} = \frac{-Z_w}{\rho S U / 2m} - C_D \tag{31}$$

Ignoring the contribution of C_D to C_{L_α}, an average $C_{L_\alpha} = 5.64$ is calculated based on the average Z_w value (Table 6). Finally,

$$
\begin{aligned}
I_{yy_{ave}} &= \frac{\rho S U c}{2M_{w_1}} C_{L_\alpha} \left(\frac{X_{\text{cg}_1} - X_{\text{np}}}{c} \right) = \frac{\rho S U c}{2M_{w_2}} C_{L_\alpha} \left(\frac{X_{\text{cg}_2} - X_{\text{np}}}{c} \right) \\
&= 27,520 \text{ slug-ft}^2
\end{aligned} \tag{32}
$$

In the case of the roll and yaw moments of inertia (I_{xx} and I_{zz}, respectively), we can use the ratio of control derivatives (L_{δ_a} and N_{δ_r}, Table 7), as well as the fact that the most significant factor contributing to the change in moments of inertia is the change in tip tank fuel mass, to determine the inertia values. Recognizing that:

$$
L_{\delta_\text{a}} = \frac{\rho S U^2 b}{2I_{xx}} C_{l_{\delta_\text{a}}} \tag{33}
$$

$$
N_{\delta_\text{r}} = \frac{\rho S U^2 b}{2I_{zz}} C_{n_{\delta_\text{r}}} \tag{34}
$$

we can use the ratio of the control derivatives to calculate the ratio of the moments of inertia between Configuration 1 and Configuration 2:

$$
\frac{L_{\delta_{\text{a}_1}}}{L_{\delta_{\text{a}_2}}} = \frac{I_{xx_2}}{I_{xx_1}} = 2.26 \tag{35}
$$

$$
\frac{N_{\delta_{\text{r}_1}}}{N_{\delta_{\text{r}_2}}} = \frac{I_{zz_2}}{I_{zz_1}} = 1.39 \tag{36}
$$

Note that several simplifying assumptions have been made here:

1. Assuming $I_{xz} \ll I_{xx}, I_{zz}$ allows us to ignore that the identified derivatives (e.g., L_{δ_a}) are actually primed derivatives:[13]

$$
L'_{\delta_\text{a}} = \frac{L_{\delta_\text{a}} + \frac{I_{xz}}{I_{xx}} N_{\delta_\text{a}}}{1 - \frac{I_{xz}^2}{I_{xx} I_{zz}}} \tag{37}
$$

2. Assuming a small trim angle of attack allows us to use the body axes identified derivatives instead of stability axes derivatives.

The change in moments of inertia between the two configurations is primarily due to the change in fuel mass in the tip tanks $\Delta m_{\text{TT}} = 44.85$ slugs (from Table 4):

$$
I_{xx_2} = I_{xx_1} + y_{\text{TT}}^2 \Delta m_{\text{TT}} + I_{xx_{\text{TT}}} \tag{38}
$$

$$
I_{zz_2} = I_{zz_1} + y_{\text{TT}}^2 \Delta m_{\text{TT}} + I_{zz_{\text{TT}}} \tag{39}
$$

where:

y_{TT} is the tip tank's lateral offset from the aircraft centerline,
$I_{xx_{\text{TT}}}$ is the tip tank's roll moment of inertia about its CG, and is assumed to be negligible (i.e., $I_{xx_{\text{TT}}} = 0$) compared to its contribution to the aircraft roll moment of inertia I_{xx} (i.e., $I_{xx_{\text{TT}}} \ll y_{\text{TT}}^2 \Delta m_{\text{TT}}$)
$I_{zz_{\text{TT}}}$ is the tip tank's yaw moment of inertia about its CG:

$$
I_{zz_{\text{TT}}} = \int_{-L_{\text{TT}}/2}^{L_{\text{TT}}/2} \frac{\Delta m_{\text{TT}}}{L_{\text{TT}}} l^2 \text{d}l \tag{40}
$$

L_{TT} is the tip tank's length along the aircraft x-axis.

Combining Equations 35 and 38 and Equations 36 and 39, we can solve for the roll and yaw moments of inertia of both configurations. The product of inertia I_{xz} was determined through trial and error of the model scaling process by comparing off-axis frequency responses (e.g., β/δ_a, p/δ_r) where its effects were most noticeable. The values of the moments of inertia for the two configurations are provided in Table 8. Note that the actual values of I_{yy} for the two configurations were slightly modified based on the model scaling process, though the average of the I_{yy} values in Table 8 matches very closely to that calculated in Equation 32.

Table 8. Calculated Moments of Inertia Based on Identified Derivatives

Moment of Inertia [slug-ft^2]	Config. 1 Light/Fwd	Config. 2 Heavy/Aft
I_{xx}	11,985	26,446
I_{yy}	26,765	27,932
I_{zz}	41,395	56,302
I_{xz}	1949.8	1341.8

C. Baselining Results

To test the ability of the stitched model to scale one loading configuration to another, the stitched model was populated with the 250 kts light-weight/forward-CG model (Configuration 1) and associated longitudinal speed stability trim data. The stitched model was then scaled to the 250 kts heavy-weight/aft-CG configuration (Configuration 2), by setting m_{sim} and I_{sim} in Figure 1 to the heavy-weight/aft-CG configuration values.

Figures 24 through 27 show comparisons of the primary on-axis frequency responses of the flight identified 250 kts heavy-weight/aft-CG model and the results of the scaled stitched model. In addition, Table 9 shows a comparison of the trim data from flight and from the scaled stitched model for the 250 kts heavy-weight/aft-CG configuration. An excellent agreement is seen in both the frequency responses (dynamic response) and trim data between the flight data and scaled stitched model. This gives confidence in the stitched model's ability to scale one loading configuration to another, which was subsequently used to scale all flight identified models to a single, common loading configuration.

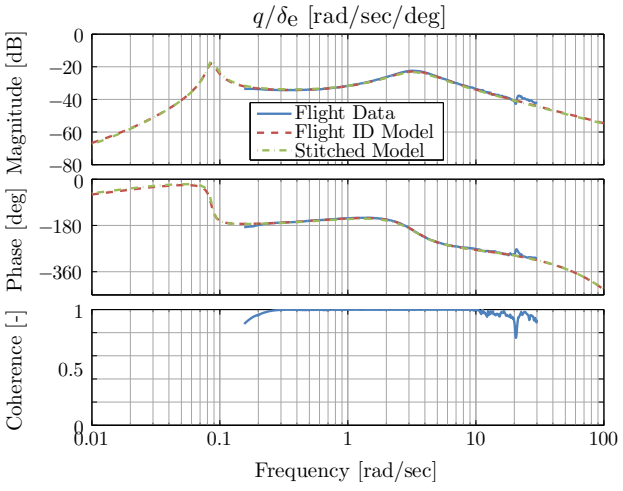

Figure 24. Pitch rate response to elevator input comparison between flight identified model and scaled stitched model (250 kts, 15,000 ft, heavy loading configuration).

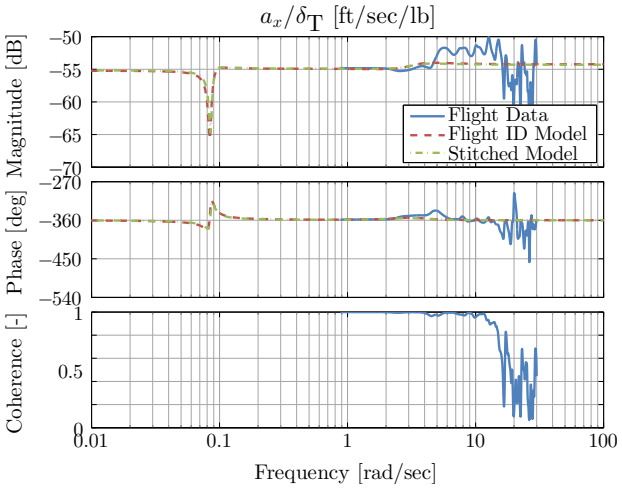

Figure 25. Roll rate response to aileron input comparison between flight identified model and scaled stitched model (250 kts, 15,000 ft, heavy loading configuration).

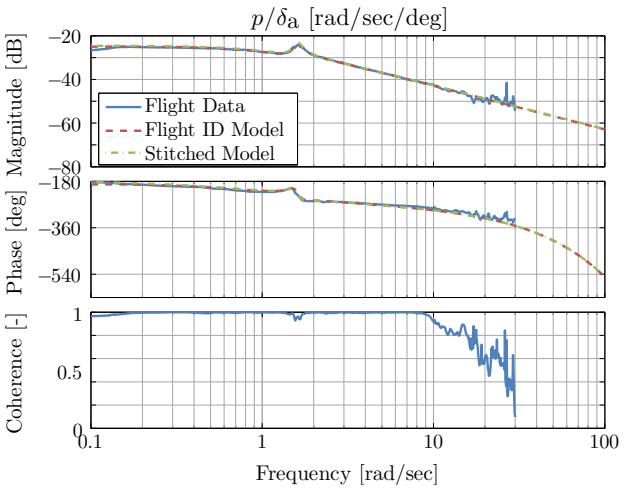

Figure 26. Roll rate response to aileron input comparison between flight identified model and scaled stitched model (250 kts, 15,000 ft, heavy loading configuration).

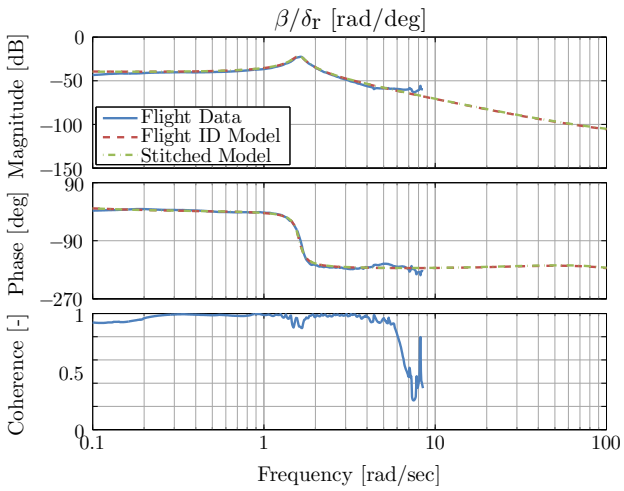

Figure 27. Sideslip response to rudder input comparison between flight identified model and scaled stitched model (250 kts, 15,000 ft, heavy loading configuration).

Table 9. Trim Comparison (250 kts, 15,000 ft, heavy loading configuration)

	Flight ID	Stitched Model
θ_0 [deg]	2.883	2.787
α_0 [deg]	2.883	2.787
δ_{e_0} [deg]	−3.968	-3.779
δ_{s_0} [deg]	0	0
δ_{T_0} [lbs]	14,559	14,376

VI. Repurposing Longitudinal Speed Stability Data

Recall from Section II.A that it is important to have a fine grid of trim data about each individual point model to accurately capture the effects of the speed stability derivatives. Therefore, in addition to scaling each identified point model to a common loading configuration, the stitched model was also trimmed at airspeeds of −20, −10, +10, and +20 kts about the trim flight condition of each point model. During this trimming process, altitude was held constant while thrust was allowed to vary, thus generating a fine grid of constant altitude trim data to be used in the complete stitched model implementation (Section II.C.3).

Figure 28 shows this process of repurposing the longitudinal speed stability data (taken by fixing throttle and varying altitude) into a set of trim shot data (holding altitude constant but varying throttle) for the 185 kts, 15,000 ft model (Point 2, Table 1, Figure 3). This is a particularly interesting point since an inflection in the trim thrust curve becomes apparent after repurposing the data, indicating the minimum drag speed for this loading configuration. Note that the trim thrust (δ_{T_0}) varies for the constant throttle data since thrust is a function of throttle, altitude, and airspeed. This process of repurposing the longitudinal speed stability trim data to constant altitude trim data was repeated for each of the identified point models.

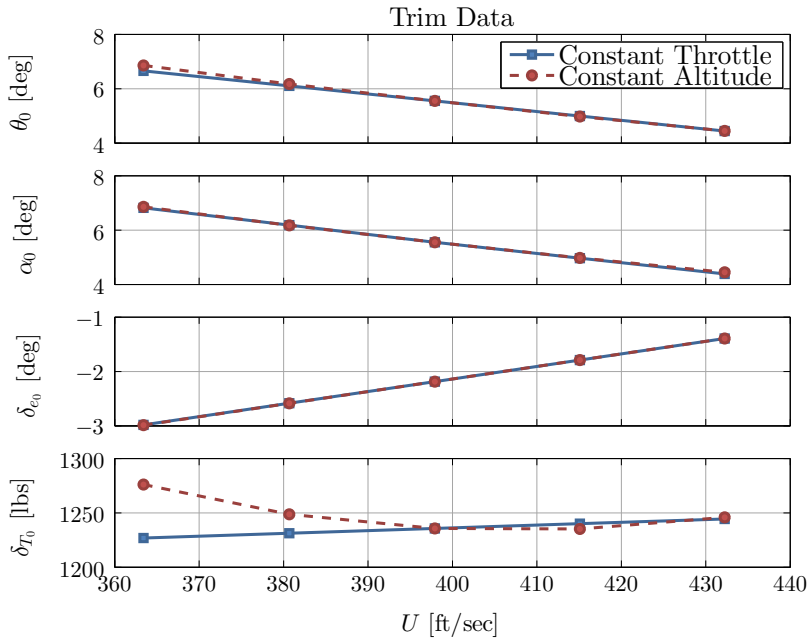

Figure 28. Longitudinal speed stability data (constant throttle, varying altitude) repurposed into constant altitude, varying thrust data for the stitched model (185 kts, 15,000 ft).

VII. Stitched Model Data

This section describes the collection of the baselined point ID models and repurposed longitudinal speed stability (LSS) data into the lookup tables in the stitched model. A smoothing process was applied to the stability and control derivatives, while the trim data were fit with linear/quadratic least squares fits to generate a finer grid of data and extend it to airspeeds beyond what was collected in flight.

A. Stability and Control Derivatives

Figures 29 and 30 show the longitudinal and lateral/directional axes stability and control dertivatives variations with the primary scheduling variable in the stitched model (i.e., x-body axis velocity U). The figures show the values of the baselined derivatives (solid blue line with squares). The error bars plotted for some derivatives are their Cramér-Rao bounds, which define the $\pm 1\sigma$ for each identified parameter.[3] Cramér-Rao bounds for the 250 kt ($U \approx 525$ ft/sec) longitudinal axis model were given in Table 3, for example. Note that all error bars are less than 10% indicating excellent parameter identification accuracy. Parameters with no error bars were fixed or eliminated during the identification process. The dashed red lines show the smoothed values that are actually implemented in the stitched model. These smoothed curves were manually selected to follow expected variations in derivatives with airspeed[2,3] and to stay within about $\pm 1\sigma$ for each parameter.

Once the stitched model was populated with the smoothed values, it was trimmed and linearized at each identification flight and loading configurations. The resulting frequency responses from the stitched model were then compared with those extracted from flight data to ensure that no errors were introduced during the smoothing process. In all cases, the linearized stitched model matched the frequency responses from flight data very closely. Some of these results are presented in Section VIII.

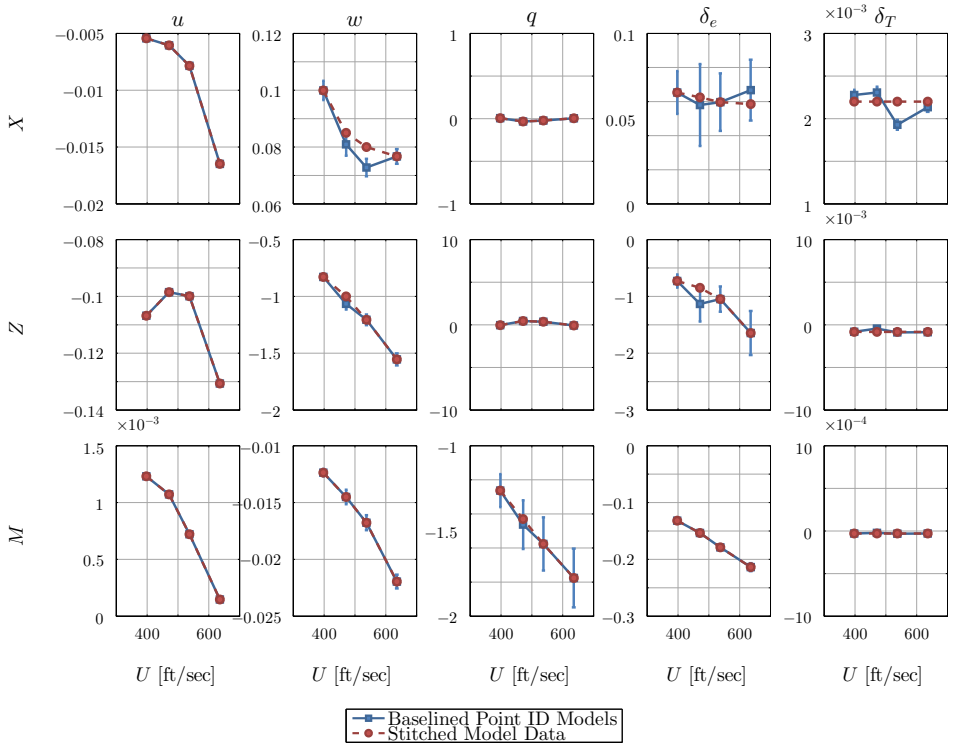

Figure 29. Longitudinal axis stability and control derivatives as a function of airspeed (15,000 ft).

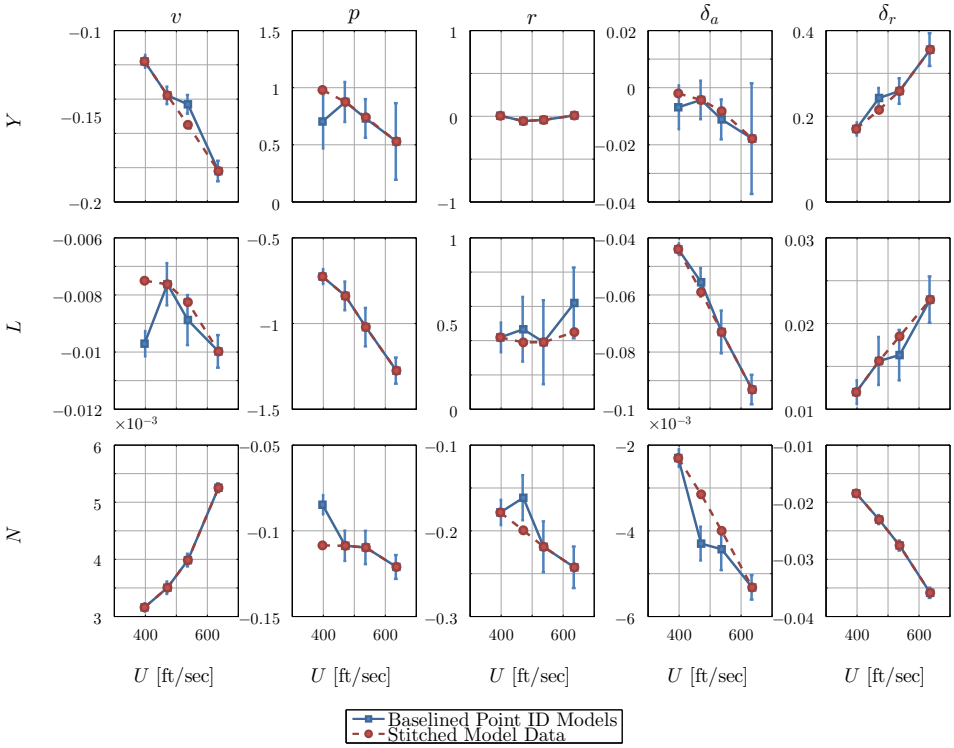

Figure 30. Lateral/directional axis stability and control derivatives as a function of airspeed (15,000 ft).

B. Trim Data

Once the LSS data set around each point model was repurposed into a constant altitude, varying thrust trim shot data set, and baselined to the stitched model loading configuration (Section VI), the four trim shot data sets were combined. Then, least squares fits were made to each trim parameter based on its expected variations with airspeed, in order to both be able to generate a finer grid of trim data and to be able to extrapolate the trim data to airspeed values above and below the existing set.

Figure 31 shows this process for trim angle of attack. Based on the relationship of lift L to angle of attack α and total airspeed V_{tot}:

$$L \propto V_{\text{tot}}^2 \alpha \tag{41}$$

and the fact that the trim data is at constant aircraft weight (and therefore constant lift), it is expected that trim angle of attack will vary linearly with $1/V_{\text{tot}}^2$.

The results shown in Figure 31 confirm that both the repurposed LSS data from the four models and the separately recorded trim shot data follow this linear trend closely. Also plotted on the figure is the linear fit that was made to the data and used to generate the finer grid of trim angle of attack which extends beyond the airspeed range of the collected data. Note that Equation 41 assumes no Mach effects, but the linear trend seen in Figure 31 confirms this assumption for this airspeed range. Similar analyses were done for the remaining trim parameters.

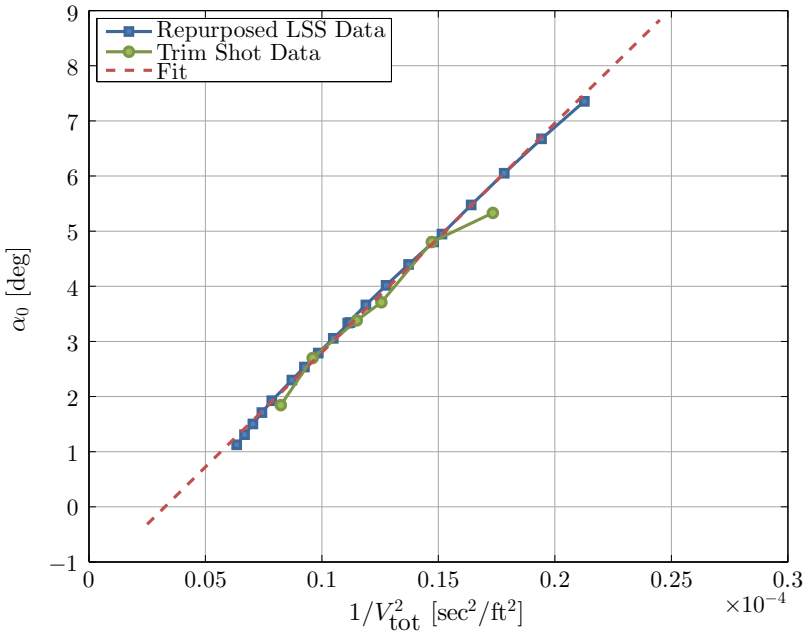

Figure 31. Angle of attack trim data spline fit and extrapolation (15,000 ft).

Figure 32 shows the stitched model trim data variations with the stitching parameter U. The stitched model trim data is overlaid with the repurposed LSS data, and trim shot data. The stitched model trim data, formed by least squares fits to the repurposed LSS data (as shown for angle of attack in Figure 31) matches the repurposed LSS data and trim shot data very closely.

Also plotted on the figure are the trim data from Point 7 [Table 1, 250 kts ($U \approx 525$ ft/sec), 15,000 ft, full tip fuel tanks]. The Point 7 data were gathered in flight at the stitched model loading configuration (and so did not require baselining). These data were not included in the development of the stitched model, but are only plotted here as a check after determining the least squares fits, and show an excellent agreement with the stitched model trim data.

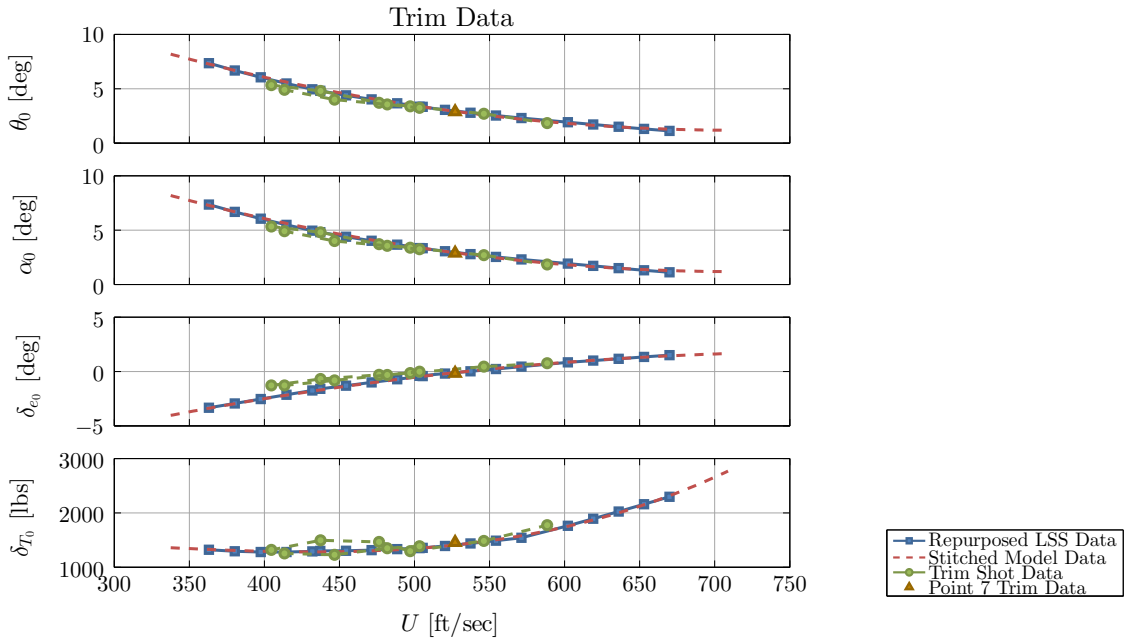

Figure 32. Trim data as a function of airspeed (15,000 ft).

C. Effects of Flaps

The stitched model data presented thus far in Sections VII.A and VII.B was for flaps up ($\delta_f = 0$). Recall from Equation 15, that the Learjet stitched model is stitched with x-body axis velocity U and scheduled with flap deflection δ_f. The stitched model requires a rectangular grid of data (i.e., there must be a corresponding flaps down model at each flaps up model U, even if some of these models are outside the flaps down flight envelope).

To populate the stitched model lookup tables with additional data for the flaps down configuration, the point model and LSS data for Point 1 (Table 1, Figure 3) were used. Scale factors were determined between the Point 1 and Point 2 identified point models (both at 185 kts, 15,000 ft but varying flap deflections). In addition, trim values and trim gradient scale factors were also determined. These stability and control derivatives, trim, and trim gradient scale factors were then used to generate $\delta_f = 20$ data from the $\delta_f = 0$ models and trim data to populate the stitched model.

VIII. Validation of Final Stitched Model

This section covers both time- and frequency-domain validation of the final stitched model using flight data that were not used for identification. The validation was done at several different flight conditions, some matching the flight conditions of the point models in the stitched model and some not. Furthermore, the validation flight data were in general recorded at loading (fuel, weight, CG) conditions different than the stitched model. Therefore, the results presented in this section will validate the ability of the stitched model to trim at and simulate conditions that require interpolation and extrapolation.

A combination of pilot stick inputs and Programmed Test Inputs (PTI) were used for the time-domain validation. The direct pilot stick to aircraft aerosurfaces connection was included in the stitched model to be able to use the recorded pilot inputs and PTIs from flight to simulate the model.

A. Doublets

Validation doublets were implemented through Programmed Test Inputs (PTI) in the VSS. To generate the stitched model results, the model was first trimmed at the same flight condition and loading configuration as the flight data. Then, the recorded PTI and pilot inputs (i.e., stick, pedals, and throttles) were used as the inputs to simulate the stitched model.

Figure 33 shows a pitch axis doublet response at the 250 kts, 15,000 ft flight condition. The first subplot shows the input force on the longitudinal stick F_{lon} from the PTI. The second subplot shows the resulting elevator deflection δ_{e} from flight data and from the stitched model. The trim elevator deflection value (first 5 sec of the plot) matches flight data, meaning the stitched model trim data is accurate. The elevator deflection during the doublet matches flight data as well, which validates the stick to elevator gain implemented in the model. The remaining subplots show the primary longitudinal aircraft responses (q, θ, n_z, and α) as measured from flight and from the stitched model. Again, the first 5 sec of the responses match well, demonstrating that the stitched model trimmed at the right aircraft states. Furthermore, the stitched model dynamic responses all match flight data very well, as indicated by the low RMS fit error cost[3] $J_{\text{RMS}} = 0.22$ for the maneuver shown. From the small negative initial pitch rate q, sloping down initial pitch attitude θ, and initial normal acceleration n_z greater than -1 g, it can be seen that the aircraft was slightly out of trim in flight. This did not negatively impact the validation.

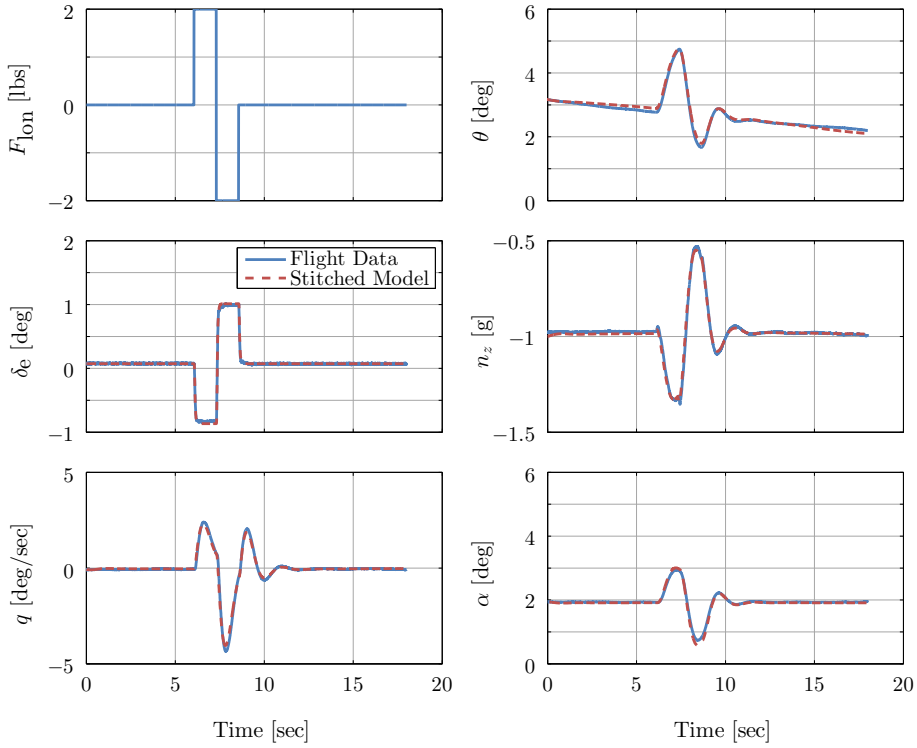

Figure 33. Pitch doublet response (250 kts, 15,000 ft).

Figure 34 shows a roll axis doublet response at the 250 kts, 15,000 ft flight condition. The first subplot shows the input force on the lateral stick F_{lat}. The second subplot shows the resulting aileron deflection δ_{a} from flight data and from the stitched model. The excellent match in aileron deflection validates the stick gain implemented in the stitched model. The remaining subplots show the primary lateral/directional aircraft responses (p, r, n_y, and β) as measured from flight and from the stitched model. As with the pitch doublet response, there is an excellent match between the stitched model and the flight data, with $J_{\text{RMS}} = 0.53$, demonstrating the stitched model's accurate representation of the aircraft roll mode and lightly damped Dutch roll mode.

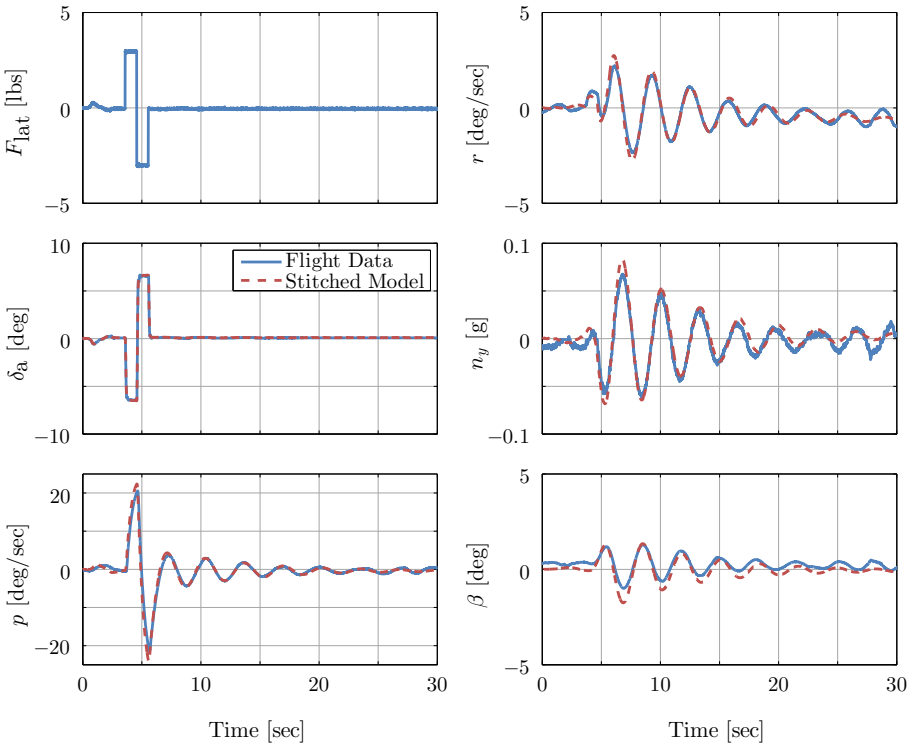

Figure 34. Roll doublet response (250 kts, 15,000 ft).

B. Elevator and Stick Force Maneuvering Stability

Elevator and stick force maneuvering stability were validated using a wind-up turn, or slowly varying g, maneuver.[10] As with the doublet data above, the stitched model results were generated by first trimming the stitched model at the same flight condition and loading configuration as the flight data, and then using the recorded pilot inputs (i.e., stick, pedals, and throttles) to simulate the stitched model. This is a very dynamic maneuver that includes banking, diving, and increasing load factor, and hence is an excellent way to validate the fidelity of the stitched model in multiple axes simultaneously.

Figure 35 shows the stick force F_{lon}, elevator deflection δ_{e}, and angle of attack α plotted against normal acceleration from flight and from the stitched model. Note that autotrim was on during this maneuver, and so the horizontal stabilizer δ_{s} moved to offload the elevator at about $n_z = 1.5$ g. This resulted in the slight change in slope of the stick force per g $\mathrm{d}F_{\text{lon}}/\mathrm{d}n_z$ and elevator per g $\mathrm{d}\delta_{\text{e}}/\mathrm{d}n_z$ seen in the figure. Below $n_z = 1.5$ g, the average stick force per g is $\mathrm{d}F_{\text{lon}}/\mathrm{d}n_z = 15.35$ lbs/g from flight data and $\mathrm{d}F_{\text{lon}}/\mathrm{d}n_z = 14.53$ lbs/g from the stitched model. The close agreement again validates the fidelity of the stitched model.

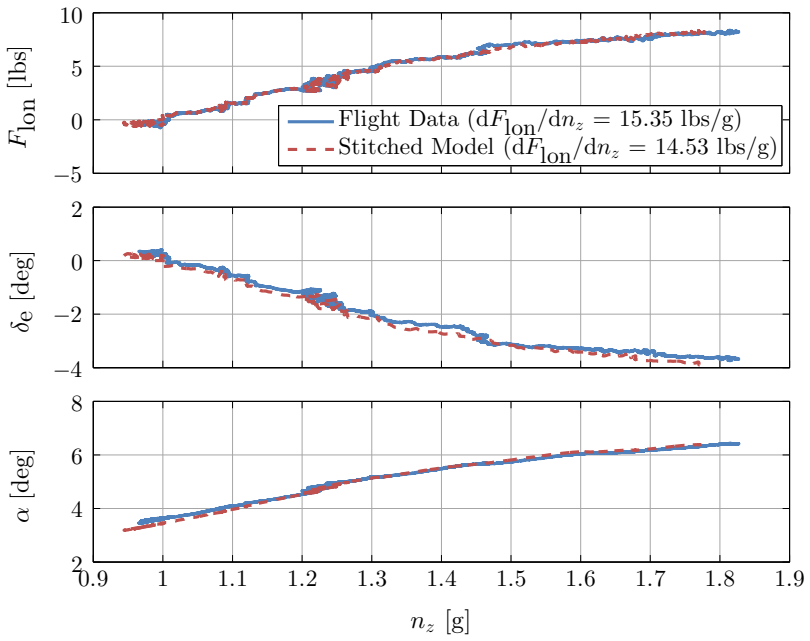

Figure 35. Wind-up turn (185 kts, 15,000 ft).

C. Roll Rate Per Aileron Deflection

Roll rate per aileron deflection was assessed in flight using PTI step inputs of varying magnitudes (1/4, 1/2, and 3/4 of full stick input) in both directions. For each input, the resulting steady-state roll rate was recorded to generate the plots in Figure 36, for the 250 kts, 15,000 ft flight condition. The figure shows the results from flight and from simulating the stitched model with the PTI inputs from flight. There is an excellent agreement between the stitched model and flight data, with both having a value of stick force per roll rate of $\mathrm{d}F_{\text{lat}}/\mathrm{d}p = 0.13$ lbs/deg/sec.

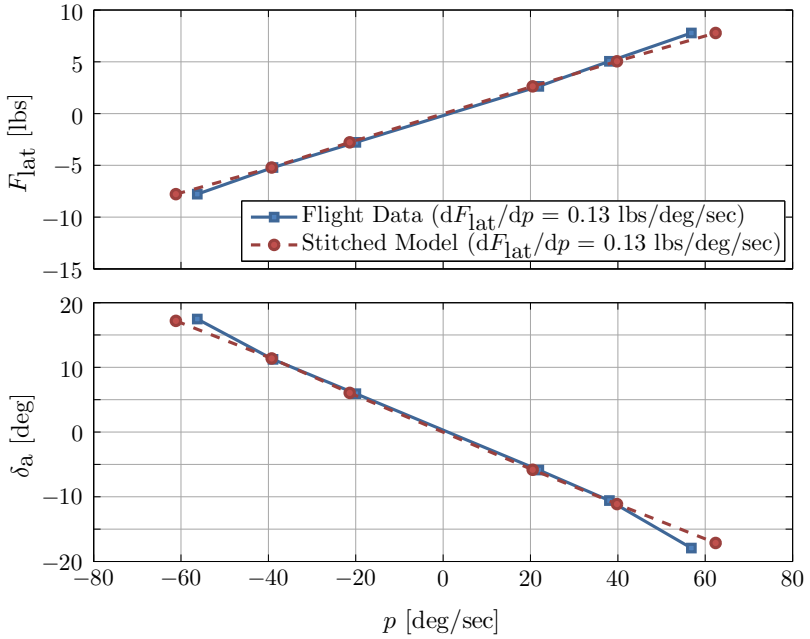

Figure 36. Roll rate per aileron deflection (250 kts, 15,000 ft).

D. Sideslip Per Rudder Deflection

Sideslip per rudder deflection was assessed in flight using a piloted steady heading sideslip maneuver. The resulting sideslip angle β, pedal force F_{ped}, and rudder deflection δ_{r} were recorded to generate the plots in Figure 37. The figure shows the results from flight and from simulating the stitched model with the piloted inputs from flight. There is an excellent agreement between the stitched model and flight data, with both having values of pedal force per sideslip $\mathrm{d}F_{\text{ped}}/\mathrm{d}\beta$ within 6%.

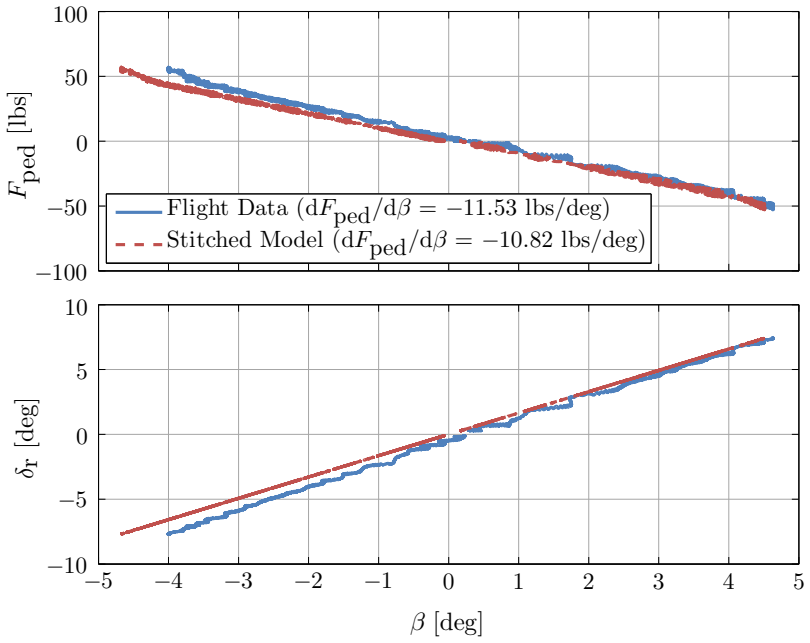

Figure 37. Steady heading sideslip (250 kts, 15,000 ft).

E. Frequency Responses

Figures 38 through 41 show frequency response comparisons from flight data and from the final stitched model for the primary on-axis responses. Flight data were analyzed in CIFER® to generate frequency responses, while results from the stitched model were obtained by trimming and linearizing the stitched model at the appropriate flight condition and loading configuration. The results were generated at 275 kts, 15,000 ft (Point 8, Table 1), which is a flight condition that does not align with any of the point models in the stitched model. Therefore, these results test the stitched model's interpolation capabilities.

Figure 38 shows the normal load factor frequency response to elevator input (n_z/δ_{e}) for both the stitched model and flight data. There is an excellent agreement over the broad frequency range of good coherence ($\gamma \geq 0.6$) $\omega = 0.2$ to 8 rad/sec. Figure 39 shows the longitudinal load factor frequency response to thrust input (n_x/δ_{T}) for both the stitched model and flight data. The flight data frequency response for thrust was generated from a thrust pulse, and not frequency sweeps, hence the frequency range of good coherence is smaller $\omega = 0.9$ to 10 rad/sec. The stitched model is an excellent match to the flight data over this frequency range.

Figure 40 and 41 show the roll rate to aileron (p/δ_{a}) and sideslip to rudder (β/δ_{r}) frequency responses, respectively. There is an excellent agreement between the stitched model and flight data for both of these lateral/directional responses.

Similar agreement between the stitched model and flight data was observed for the other aircraft responses. These results validate the ability of the stitched model to accurately simulate the aircraft dynamics at flight conditions not explicitly included in the stitched model data.

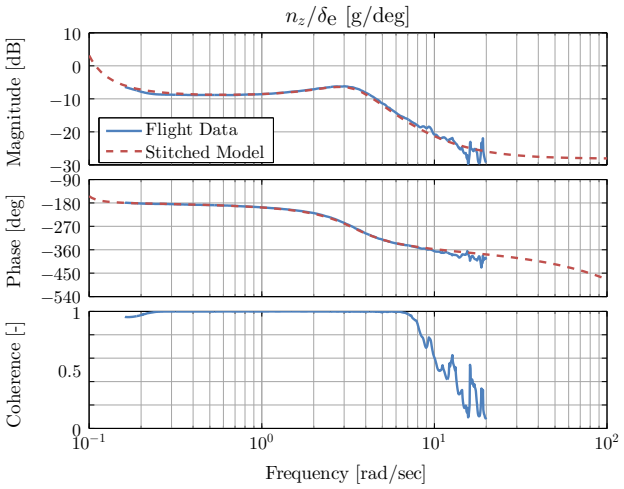

Figure 38. Normal acceleration response to elevator input (275 kts, 15,000 ft).

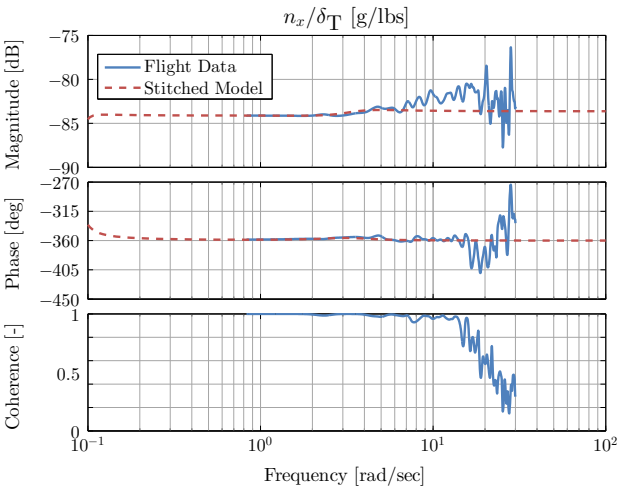

Figure 39. Longitudinal acceleration response to thrust input (275 kts, 15,000 ft).

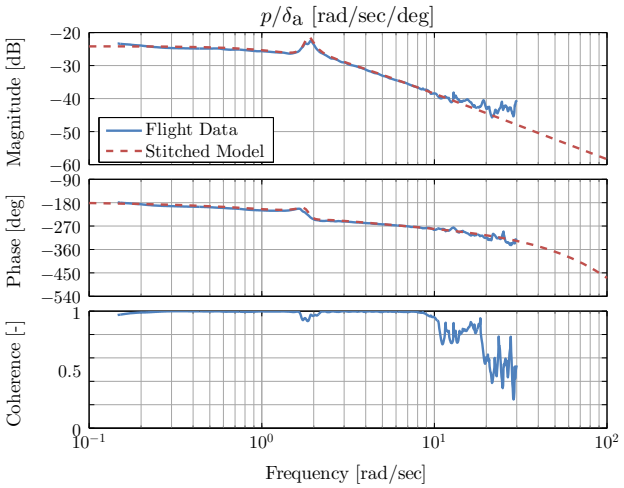

Figure 40. Roll rate response to aileron input (275 kts, 15,000 ft).

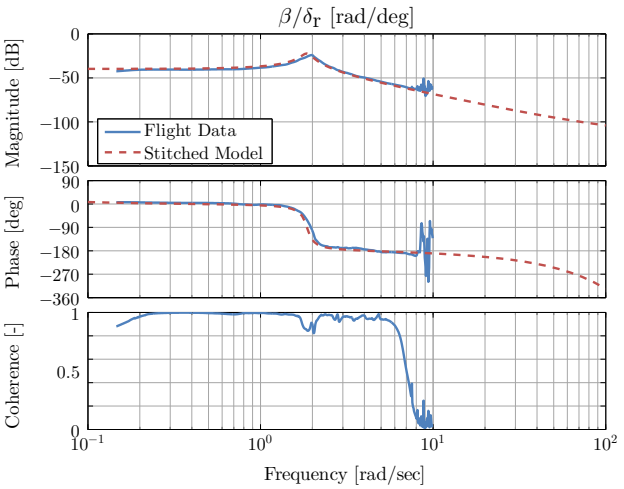

Figure 41. Sideslip response to rudder input (275 kts, 15,000 ft).

F. Flaps

Figure 42 shows a piloted pitch axis doublet response at the 140 kts, 10,000 ft, flaps 20, and gear down flight condition. The first subplot shows the input force on the longitudinal stick F_{lon} from the pilot. The second subplot shows the resulting elevator deflection δ_e from flight data and from the stitched model. The trim elevator deflection value (first 5 sec of the plot) matches flight data very closely, meaning the stitched model trim data is accurate. The remaining subplots show the primary longitudinal aircraft responses (q, θ, n_z, and α) as measured from flight and from the stitched model. Again, the first 5 sec of the responses match well, demonstrating that the stitched model trimmed at the right aircraft states for this flight condition. Furthermore, the stitched model dynamic responses all match flight data well. This validates the stitched model's capability to schedule with flap deflection and to extrapolate to a lower airspeed and altitude than the models used to develop the stitched model.

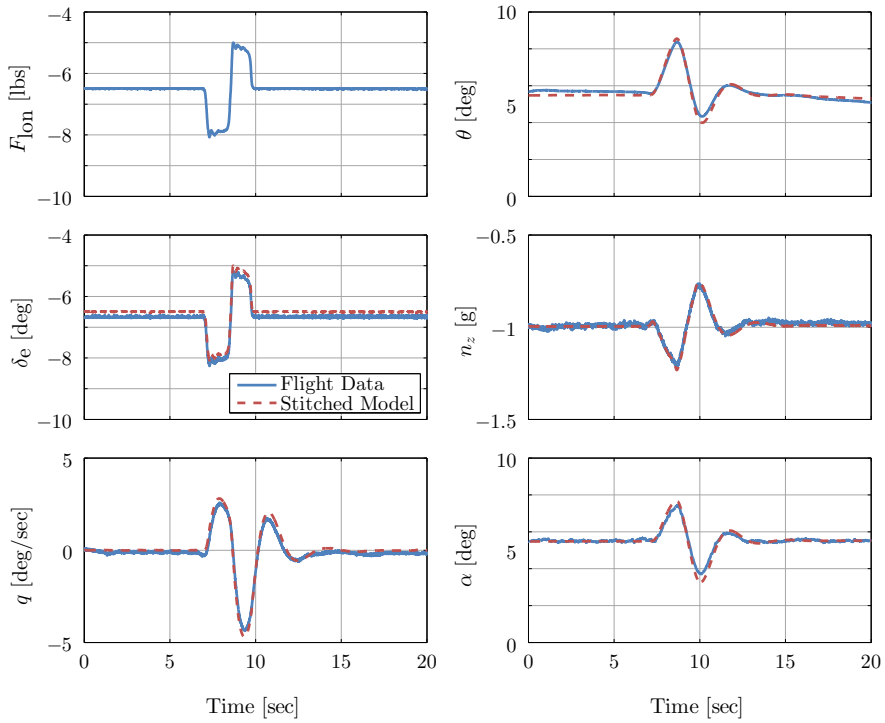

Figure 42. Pitch doublet response (140 kts, 10,000 ft, flaps 20/gear down).

IX. Conclusions

1. An overview of the model stitching was presented, beginning with a brief background to qLPV modeling. The importance of accurate trim data was highlighted to ensure the fidelity of the parameters in the model that are preserved through trim gradients. Specific aspects of the stitched model were highlighted which make it a useful application of qLPV modeling to aircraft and rotorcraft applications.

2. A flight test was carried out on the Calspan VSS Learjet-25 to gather flight data for system identification of state-space models at several flight conditions and loading configurations. An example identification of a longitudinal axis state-space model was presented, including a method for using longitudinal speed stability data to determine and fix speed derivatives that would otherwise be insensitive and difficult to identify.

3. A method for scaling flight identified models from the loading configuration at which they were identified to a different loading configuration was presented. This scaling method was then tested at a single flight condition at which models at two different loading configurations were identified. A light-weight/forward-CG model was scaled to a heavy-weight/aft-CG configuration. The scaled light model showed an excellent match to the heavy model in both the dynamic response (frequency responses) as well as trim data. This scaling method was used to baseline flight identified models at a variety of different loading configurations to a common loading configurations. As part of this process, a method to repurpose and baseline LSS data was presented.

4. The baselined stability and control derivatives and trim data were implemented in the final stitched model which was then validated against flight data at flight conditions and loading configurations different from those used in the stitched model. Validation included frequency response comparisons and time history comparisons in the form of doublet responses and stick gradient checks. All validation checks showed good agreement between the stitched model and flight data.

5. These results show the excellent ability of the stitched model to accurately simulate the aircraft over its full flight envelope, using only a limited number of identified point models at a single altitude. This model is now in use at the USAF TPS flight simulator laboratory.

Acknowledgments

The authors would like to thank Evan Thomas, Jason Kirkpatrick, Jay Kemper, and Ryan McMahon (Calspan Corporation) for their hard work on the flight tests and simulator integration.

References

[1]Zivan, L. and Tischler, M. B., "Development of a Full Flight Envelope Helicopter Simulation Using System Identification," Journal of the American Helicopter Society, Vol. 55, No. 022003, pp. 1-15, 2010.

[2]Tobias, E. L. and Tischler, M. B., "A Model Stitching Architecture for Continuous Full Flight-Envelope Simulation of Fixed-Wing Aircraft and Rotorcraft from Discrete-Point Linear Models," U.S. Army AMRDEC Special Report RDMR-AF-16-01, April 2016.

[3]Tischler, M. B. and Remple, R. K., *Aircraft and Rotorcraft System Identification: Engineering Methods and Flight Test Examples Second Edition*, AIAA, 2012.

[4]Berger, T., Tischler, M. B., Hagerott, S. G., Cotting, M. C., Gresham, J. L., George, J. E., Krogh, K. J., D'Argenio, A., and Howland, J. D., "Handling Qualities Flight Test Assessment of a Business Jet N_zU P-β Fly-By-Wire Control System," AIAA Atmospheric Flight Mechanics, Grapevine, TX, January 2017.

[5]Kemper, J. and Cotting, M. C., "Simulator Design for Flying and Handling Qualities Instruction," AIAA Modeling and Simulation Technologies Conference, San Diego, CA, January 2016.

[6]Tobias, E. L., Tischler, M. B., Berger, T., and Hagerott, S. G., "Full Flight-Envelope Simulation and Piloted Fidelity Assessment of a Business Jet Using a Model Stitching Architecture," presented at the AIAA Modeling and Simulation Technologies Conference, Kissimmee, FL, January 2015.

[7]Marcos, A. and Balas, G. J., "Development of Linear-Parameter-Varying Models for Aircraft," AIAA Journal of Guidance, Control, and Dynamics, Vol. 27, No. 2., March-April 2004.

[8]Lawrence, B., Malpica, C. A., and Theodore, C. R., "The Development of A Large Civil Tiltrotor Simulation for Hover and Low-Speed Handling Qualities Investigations," presented at the 36th European Rotorcraft Forum, Paris, France, September 2010.

[9]Lawrence, B., Berger, T., Tischler, M. B., Elmore, J. amd Gallaher, A., Theodore, C. R., and Tobias, E. L., "Integrating Flight Dynamics and Control Analysis and Simulation in Rotorcraft Conceptual Design," presented at the American Helicopter Society 72nd Annual Forum, West Palm Beach, FL, May 2010.

[10]Kimberlin, R. D., *Flight Testing of Fixed-Wing Aircraft*, AIAA, 2003.

[11]Gresham, J. L., George, J. E., Krogh, K. J., D'Argenio, A., and Howland, J. D., "Limited Evaluation of Cessna Aircraft Company Control Law (Project Tacit CLEAR)," USAF TPS-TIM-15B-02, June 2016.

[12]Anon., "U.S. Naval Test Pilot School Flight Test Manual: Fixed Wing Stability And Control Theory and Flight Test Techniques," USNTPS-FTM-No. 103. Naval Air Warfare Center, Aircraft Division, Patuxent River, MD, January 1997.

[13]McRuer, D., Ashkenas, I., and Graham, D., *Aircraft Dynamics and Automatic Control*, Princeton University Press, 1990.